RSC Advances

PAPER

View Article Online
View Journal | View Issue

Cite this: *RSC Adv.*, 2025, **15**, 16742

Green synthesis of ZnO nanoparticles using *E. cardamomum* and zinc nitrate precursor: a dual-functional material for water purification and antibacterial applications

Harpreet Kaur,*[a] Abhishek Sharma,[b] Krishna Anand,[b] Ankush Panday,[b] Shavan Tagotra,[b] Sachin Kakran,[b] Anuj Kumar Singh,[b] Mir Waqas Alam,[c] Sanjeev Kumar,*[a] Gassoumi Bouzid,[d] Jasvir Dalal*[e] and Gurjinder Singh[f]

This study presents an eco-friendly, bio-engineered approach for synthesizing zinc oxide nanoparticles (ZnO NPs) using *Elettaria cardamomum* pod (*EC*-pod) extract, offering a sustainable alternative for environmental remediation and antimicrobial applications. X-ray diffraction (XRD) analysis confirms the wurtzite crystalline phase, with an average particle size of 20.87 nm. Ultraviolet-visible (UV-Vis) spectroscopy reveals a characteristic absorption peak at 372 nm, corresponding to an energy band gap of 3.33 eV. Fourier-transform infrared (FTIR) spectroscopy highlights the role of phytochemicals as capping and stabilizing agents. Field emission scanning electron microscopy (FESEM) and high-resolution transmission electron microscopy (HRTEM) confirm multi-architectural morphologies, including hexagonal, spherical, rod-like, and pentagonal structures, with energy-dispersive X-ray (EDX) spectroscopy verifying elemental purity. The photocatalytic efficiency of *EC*-pod:ZnO in degrading malachite green (MG) dye under UV irradiation reaches 99.8% removal within 160 minutes, with a high quantum yield of 2.73×10^{-3} molecules per photon and a space-time yield of 1.37×10^{-5} molecules per photon per mg. Additionally, *EC*-pod:ZnO exhibits significant antibacterial activity against both Gram-positive (*Staphylococcus aureus*) and Gram-negative (*Pseudomonas aeruginosa*) bacteria, showcasing its dual functionality as a potential photocatalyst and antimicrobial agent. This nature-inspired ZnO nanomaterial offers an economical, scalable, and sustainable solution for environmental and biomedical applications, highlighting its potential in wastewater treatment and microbial control.

Received 1st March 2025
Accepted 8th May 2025

DOI: 10.1039/d5ra01469g

rsc.li/rsc-advances

1 Introduction

Azo dye contamination in wastewater alters water chemistry, increases oxygen demand, and poses toxicity risks to aquatic life and human health.[1] Their discharge into water bodies can degrade water quality, disrupt aquatic systems, and potentially affect soil properties and crop productivity. Such pollution adds to the growing environmental pressures that threaten aquatic life, human health, water resources, and agricultural systems. In light of these challenges, the adoption of sustainable, low-impact treatment strategies becomes essential.[2–4] This emphasizes the urgent need for effective wastewater treatment. To address the critical challenge of wastewater treatment, a range of conventional methods has been utilized to mitigate pollutant levels effectively. These methods include chemical treatments like chlorination and ozonation, biological methods involving microbial degradation, and physical processes such as adsorption and coagulation.[5–7] While effective to some extent, these approaches have significant limitations. Chemical methods often lead to the formation of secondary pollutants and incur high operational costs. Biological methods are limited by their ineffectiveness in treating non-biodegradable contaminants, while physical processes are often energy-intensive and do not completely degrade toxic compounds.[5,8] These challenges necessitate the development of advanced and sustainable alternatives for wastewater remediation.

Nanotechnology-based solutions, such as photocatalytic degradation using nanoparticles, offer a promising alternative

[a]*Department of Physics, Chandigarh University, Gharuan Mohali, 140413, India. E-mail: mann.khant91@gmail.com; kumarsanju25@gmail.com*

[b]*University Institute of Engineering, Chandigarh University, Gharuan Mohali, 140413, India*

[c]*Department of Physics, College of Science, King Faisal University, Al-Ahsa 31982, Saudi Arabia*

[d]*Laboratory of Advanced Materials and Interfaces (LIMA), University of Monastir, Faculty of Science of Monastir, Avenue of Environment, 5000, Monastir, Tunisia*

[e]*Department of Physics, Rajdhani College, University of Delhi, Delhi – 110015, India. E-mail: jasvirdalal2012@gmail.com*

[f]*Department of Electrical and Electronics and Communication Engineering, DIT University, Dehradun-248009, India*

Table 1 Reports on the eco-friendly and green synthesis of ZnO NPs using biomolecules of different plant extracts

Sr. no.	Year	Plant	Part used	Particle-size	Particle-shape	Application	Reference
1	2024	*Epipremnum aureum*	Leaf	29 nm	Spherical	Photocatalytic activity	13
2	2024	*Eucalyptus globulus*	Leaf	25–151 nm	Spherical	Photocatalytic activity	14
3	2024	*Ephedra alata*	Leaf	5–30 nm	Spherical	Photocatalytic activity	15
4	2023	Banana	Peel	57.4 ± 13.8 nm	Spherical	Antimicrobial activity	16
		Date	Seed	72.6 ± 17.1 nm			
5	2023	*Punica granatum*	Peel	49.52 nm	Spherical	Antioxidant and catalytic activity	17
6	2023	*Ocimum lamifolium*	Leaf	6.5–22.8 nm	Spherical	Electrochemical and antibacterial activity	18
7	2023	*Cnidoscolus aconitifolius*	Leaf	100 nm	Spherical	Anti-inflammatory and antibacterial	19
8	2022	*Anisomeles malabarica*	Leaf	1.5–8.5 nm	Spherical	—	20
9	2022	*Cocos nucifera*	Leaf	16.6 nm	Flower shaped	Antimicrobial, antioxidant and photocatalytic activity	21
10	2022	*Pomegranate* solid coffee	Peel	111–118 nm	Hexagonal and nanorod shape	Antibacterial activity	22
11	2022	*Raphanus sativus*	Leaf	66.47 nm	Spherical	Anticancer and antibacterial activity	23
12	2021	*Piper betle*	Leaf	112 nm	Spherical	Antibacterial	24
13	2021	*Rubus fairholmianus*	Root	100 nm	Spherical	Antibacterial activity	25
ZnO using *E. cardamomum* extract							
14	2020	*EC*	Seed	1.77 ± 2.3 nm	Rod shape	Anticancer and antibacterial activity	26
15	2020	*EC*	Seed	18.72 nm	Spherical	Larvicidal and antibacterial activity	27
16	2020	*EC*	Fruit	20–100 nm	Spherical	Antifungal activity	28
17	2024	*EC*	Pod	9–71 nm	Pentagons, hexagons, spheres, capsule/rod-like, hexagonal-prism, triangular-prism, and cubes	Photocatalytic activity, antibacterial activity	Present work

due to their high efficiency in mineralizing a wide range of organic pollutants into harmless end products.[9] Nanomaterials have emerged as particularly effective photocatalysts owing to their superior light absorption, charge carrier dynamics, and chemical stability. With nanoparticles possessing special qualities because of their high surface-to-volume ratio, the development of nanotechnology has created new opportunities in several sectors, including biology, chemistry, and medicine.[10] While there are several techniques for synthesizing nanoparticles, including hydrothermal synthesis and sol–gel techniques, these procedures often need hazardous chemicals, specialized labor, and specialized equipment, which may provide difficulties and environmental dangers. Utilizing plant extracts or microorganisms, biogenic synthesis techniques have gained popularity as they offer a sustainable and eco-friendly alternative to conventional chemical synthesis methods. Green synthesis (including plant extracts) limit environmental effects due to availability of natural reducing and capping agents in the plant extracts which lessens the dependency on hazardous chemicals.[11] Furthermore, the byproducts generated are biodegradable, making this method less harmful to ecosystems compared to conventional methods.

Metal oxide nanoparticles, especially zinc oxide nanoparticles (ZnO NPs), have become increasingly common in recent research because they can be used in many different areas.[12] To synthesize ZnO NPs, different plant products from plants like *Catharanthus roseus*, *Punica granatum*, *Ocimum lamifolium*, *Cnidoscolus aconitifolius*, *Camellia sinensis*, and others were used for different purposes, as shown in Table 1.

The extract of *Elettaria cardamomum* (*EC*), which is an aromatic plant also known as the "Queen of Spices," received an extensive amount of attention for the different ways it could be used.[29] *EC* extract has many phytochemicals with antibiotic, antifungal, and antioxidant, which makes it a good material for making nanoparticles.[26,27] These phytochemicals act as reducing agents, facilitating the conversion of metal salts into NPs, and as capping agents, stabilizing the NPs and preventing aggregation. In the synthesis of metal/metal oxide NPs, these phytochemicals eliminate the need for hazardous chemical reducing and capping agents, making the process eco-friendly. Additionally, the antibiotic and antifungal components contribute to the antimicrobial potential of the NPs, while antioxidants regulate oxidation during synthesis, influencing NPs size and morphology. Thus, using plant extract, this synthesis approach enhances the environmental and biomedical applications of the NPs. Previous studies have shown that *EC*-mediated NPs, such as gold (Au), silver (Ag), titanium dioxide (TiO_2), and zinc oxide (ZnO), are useful for several biological tasks.[26,27,30,31] Some phytochemicals found in *EC* extract are very important for the production of ZnO. Phytochemicals are chemicals that plants naturally produce. Even though phytonutrients aren't considered necessary nutrients like vitamins and minerals, they are good for human health. For plants, phytochemicals are often protection systems that keep them safe from things like pests, ultraviolet (UV) rays, and diseases. Rodríguez-Negrete *et al.*, (2024) stated that antioxidants can improve health in many ways when eaten by people, such as by fighting inflammation and free radicals. Flavonoids, carotenoids, phenolic acids, and alkaloids are all popular types of phytochemicals. Rodríguez-Negrete *et al.* reported that phytochemicals can be found in large amounts in fruits, veggies, whole grains, nuts, seeds, and plants.[32] The part-specific approach in green synthesis is gaining attention because different anatomical regions of a plant such as leaves, roots, seeds, pods, and bark, contain distinct secondary metabolites in varying concentrations.[33,34] For example, seeds may be rich in fatty acids, while pods often contain volatile oils and terpenoids that provide excellent capping behaviour and influence nanoparticle morphology.[35] There are many different phytochemicals in *EC*, including camphor, borneol, α-terpineol, limonene, and 1,8-cineole.[26] It smells very different because of a mix of 1,8-cineole and *p*-menth-1-en-8-yl acetate.[36] These phytochemicals have functional groups like hydroxyl, carboxyl, and amino groups that can successfully combine with metal ions, helping to reduce them and control the particle size and shape, which in turn affects the performance of the produced NPs.[11]

However, there is limited investigation of *EC* extract for the synthesis of ZnO NPs. In the existing literature, only three studies have investigated the utilization of *EC*-seed extract in conjunction with ZnO for antibacterial, anticancer, and larvicidal activities.[26–28] However, to date, there is a notable absence of research concerning the utilization of *EC*-pod extract in mediating the synthesis of ZnO. Furthermore, investigations into the photocatalytic potential of ZnO NPs employing extracts from any part of the *EC* plant have yet to be reported in the literature. Therefore, this study investigates the potential role of *EC*-pod extract as a viable candidate for ZnO synthesis, potentially serving as an effective photocatalyst. This study aims to fill this gap by investigating the synthesis of *EC*-pod extract-mediated ZnO NPs and assessing their photocatalytic activity. Particularly, this research marks the first report of *EC*-pod extract-mediated ZnO NP synthesis, contributing to the advancement of knowledge in this area. Additionally, the study explores the novel use of *EC*:ZnO NPs in photocatalytic applications, addressing important environmental challenges such as the degradation of pollutants and water purification. Also, the antibacterial activity of *EC*-pod:ZnO is tested against Gram-positive (*Staphylococcus aureus*) and Gram-negative (*Pseudomonas aeruginosa*) bacteria.

2 Experimental details

2.1 Materials and chemicals

Sigma-Aldrich (Germany) provides high-purity ingredients that are used in the synthesis of *EC*-pod:ZnO. Zinc nitrate hexahydrate ($Zn(NO_3)_2 \cdot 6H_2O$, >99%) is used as a primary component along with ethanol (C_2H_6O, 99.5%). *EC* was collected from the plants near Chandigarh University (Punjab, India, 30.7688° N, 76.5754° E).

For photocatalytic activity, Malachite green (MG, $C_{23}H_{25}ClN_2$, molecular weight: 364.9 g mol^{-1}) used as a model pollutant with specific scavengers; isopropanol (IPA, $(CH_3)_2$-CHOH, molecular weight: 60.10 g mol^{-1}, ≥97%), ethylenediaminetetraacetic acid disodium (EDTA-2Na, $C_{10}H_{14}N_2Na_2O_8 \cdot 2H_2O$, molecular weight: 372.24 g mol^{-1},

≥99%), and benzoquinone (BQ, $C_6H_4(=O)_2$, molecular weight: 108.09 g mol^{-1}, ≥98%) were procured from Sigma-Aldrich, Germany. For antibacterial testing of Gram-positive (*Staphylococcus aureus* (MTCC 3160)), Gram-negative (*Pseudomonas aeruginosa* (MTCC 424)) bacterial strains, Nutrient agar of HiMedia, (Mumbai, India) and Petri dishes of Sigma-Aldrich, were used.

2.2 Extract preparation using *EC*-pods

To separate beneficial chemicals from *EC* pods, a careful extraction procedure was used.[30] First, pure water was used to wash the pods well and get rid of any dirt or waste that was stuck to them. After that, they were dried in the sun to get rid of any remaining water, which made grinding easier. The pods were ground into a fine powder with a pestle and mortar after they were fully dry. This made the plant matter's surface area larger which made solvent extraction work better. After measuring out 5 grams of the crushed material, it was added to a container full of pure water to start the extraction process. The mixture was slowly heated to a controlled range of 65–70 °C using a REMI stirrer-heater apparatus. It was then kept at a soft boil for 60 minutes. This longer heating time made it easier for the beneficial components to be released and dissolved in the solvent, which increased the extraction's output and effectiveness. After the extraction, the solution was left to cool down to room temperature on its own so that heat-sensitive molecules wouldn't break down. After the solution had cooled, it was filtered through Whatman filter paper to get rid of any particles that had not been wiped out. This made sure that the extract was clear and clean. The finished mixture was a light green color, which showed that beneficial phytochemicals like chlorophyll and other plant colors were present.

2.3 Synthesis of *EC*-pod:ZnO NPs

The synthesis of ZnO NPs was initiated by preparing a solution by thoroughly mixing 2.3 g of $Zn(NO_3)_2 \cdot 6H_2O$ in 150 mL of distilled water (using a stirrer), following a previously published route.[37] The solution was slowly supplemented with an aqueous extract of *EC* pod while being constantly stirred after a 10 minute interval. The successful production of NPs was shown by a noticeable change in color from translucent to white. Then, a filtration procedure was used to separate the NPs that had precipitated. After filtering, the precipitates were carefully washed with ethanol. Centrifugation at 12 000 rpm was performed five times to remove ionic contaminants for complete purification. The cleaned precipitates were allowed to dry naturally overnight before being calcined for 8 hours at 80 °C. The NPs were ground into a fine powder after the calcination procedure. This completed the synthesis, which yielded ZnO NPs made from the extract of *EC* pods.

2.4 Materials characterizations

To investigate the properties of *EC*-pod:ZnO, various characterization tools have been employed in the study. The crystal morphology of the synthesized *EC*-pod:ZnO was analyzed using X-ray powder diffraction (XRD) on a Bruker AXS-D8 diffractometer (USA). The instrument utilized Cu-Kα radiation with a wavelength of 1.54 Å and scanned within the 2θ range of 30–80° at a speed of 1 s per step, operating at 35 kV. For XRD analysis, 20 mg of *EC*-pod:ZnO was used. To observe the absorbance spectra and band gap of *EC*-pod:ZnO, an Ultraviolet-visible (UV-vis) spectrophotometer (UV-2600) of Shimadzu (Japan), was utilized in the wavelength range of 300–600 nm. For UV-Vis spectroscopy, 1 mg of *EC*-pod:ZnO powder was dispersed in solvent to form a homogeneous suspension and, then used for the absorbance analysis. Fourier transform infrared (FTIR-8400) spectrometer of Shimadzu (Japan), was used with a scanning range of 500 to 4000 cm^{-1} to identify the functional groups present in *EC*-pod:ZnO and *EC* pod extract. For FTIR analysis, a small amount of powdered sample was thoroughly mixed with spectroscopic-grade potassium bromide (KBr) in a dry environment and then pressed into a transparent pellet using a hydraulic press. While, analysis of *EC* extract was carried out in liquid form and its 2–3 drops were used. For morphological analysis and particle-size determination, the field emission scanning electron microscope (FE-SEM, Supra-55VP) of Carl Zeiss (Germany) and the high-resolution transmission electron microscope (HRTEM, Jem-2100) of Jeol (Japan), were employed along with energy dispersive X-ray spectrum (EDX) and selected area diffraction (SAED) pattern. For FESEM analysis, a suspension of 2 mg of *EC*-pod:ZnO was prepared, and a few drops were deposited onto a conductive substrate (gold), followed by drying for the proper adhesion and imaging. Similarly, for HRTEM analysis, a suspension containing 2 mg of *EC*-pod:ZnO was prepared in a solvent, and a few drops of this suspension were drop-cast onto a carbon-coated copper grid and dried prior to imaging. Thermogravimetric analysis (TGA) was performed using a TG/DTA analyzer (DTG-60H, Shimadzu, Japan) under nitrogen atmosphere to evaluate the thermal stability of *EC*-pod:ZnO. The surface charge of the *EC*-pod:ZnO NPs was determined using a Litesizer DLS 500 instrument (Anton Paar, Software version 3.4.4, Serial No. 83881800). For zeta analysis, a suspension of 1 mg of *EC*-pod:ZnO was prepared in 10 mL of distilled water. The measurements were carried out using distilled water as dispersing medium, with a refractive index of 1.33. The instrument was operated in automatic adjustment mode with a maximum applied voltage of 200 V. Manual run mode was selected, with up to 160 runs to ensure data accuracy.

2.5 Evaluation of photocatalytic activity of *EC*-pod:ZnO NPs

The photocatalytic activity of *EC*-pod:ZnO NPs was tested in the degradation of MG dye serving as a model pollutant. UV light was employed for the experiment. The initiation of the reaction involved the dispersion of 10 and 20 mg of *EC*-pod:ZnO NPs into a dye solution. Following this, the mixture was stirred using a magnetic stirrer (REMI) in the dark for 60 minutes to establish an adsorption–desorption equilibrium. Notably, UV-vis absorption spectra were recorded for initial dye concentration, and after adsorption of dye in dark conditions. UV-Vis spectra for MG dye were focused at 625 nm. The subsequent phase of the experiment involved stirring the solution under light exposure. At intervals of 10 minutes, 3 mL of the suspension was

withdrawn up to 160 and 240 minutes and after centrifuging it for the removal of the photocatalyst, the respective UV-Vis spectra were obtained for the transparent dye solution to observe the absorbance of peaks. These peaks were used to calculate the concentration of dye in water at time '*t*' and subjected to further analysis of dye removal efficiency of *EC*-pod:ZnO using the following equation:[30]

$$\text{Removal efficiency of } EC\text{-pod:ZnO} = ((X_0 - X_t)/X_0) \times 100 \quad (1)$$

Here, X_0 and X_t are the concentrations at the initial stage and time t. Further, to determine the performance of *EC*-pod:ZnO photocatalyst, the quantum yield (Q. Y.), photon flux, and space-time-yield (S. T. Y.) values were evaluated using the following equations:[38]

$$\text{Q. Y.} = \frac{\text{dye decay rate (number of molecules degraded per second)}}{\text{photon flux (photon per second)}} \quad (2)$$

$$\text{Photon flux} = (\text{number of photons per s}) \times (\text{exposure time}) \quad (3)$$

Here,

$$\text{Number of photons per s} = (\text{lamp power})/(\text{photon energy}) \quad (4)$$

Here, the dye decay rate was determined from the change in dye concentration over time, monitored using UV-Vis absorption spectra. The number of molecules degraded was calculated using the pollutant molecular weight, Avogadro's number, and pollutant mass in solution considering the initial and final concentrations over the irradiation period. Whereas, the photon flux was determined by considering the lamp power, photon energy, and light wavelength. Photon energy is given by:

$$E = hc/\lambda \quad (5)$$

Here, E is the photon energy, h is Planck's constant (6.626×10^{-34} J s), c is the speed of light (3×10^8 m s^{-1}), and λ is the wavelength of incident light.

The calculation assumes pseudo-first-order reaction kinetics, uniform light distribution over the entire reaction area, complete photon utilization in the photocatalytic process, negligible scattering and reflection losses, and a well-stirred system ensuring uniform exposure.

$$\text{S. T. Y.} = \text{Q. Y./photocatalyst } (EC\text{-pod:ZnO}) \text{ mass (mg)} \quad (6)$$

Here, S. T. Y. explicates the reduction in the number of catalytic sites due to the mass of *EC*-pod:ZnO mass utilized in the photocatalytic procedure and highlights the optimized use of catalytic resources within the reaction environment.

2.6 Mineralization and total organic carbon (TOC) analysis

Decolorization of dye solutions does not necessarily indicate complete breakdown into environmentally benign substances, such as carbon dioxide and water. Therefore, evaluating the degree of mineralization is essential for a comprehensive understanding of the treatment process. Total organic carbon (TOC) content in the MG dye solution both before and after irradiation, is estimated for the residual organic carbon – a critical indicator of the remaining organic matter, using a spectrophotometer.

2.7 Identification of active species

To understand the mechanisms behind the photocatalytic degradation process, we investigated the role of specific reactive species potentially involved. These species, including hydroxyl radicals ($\cdot$OH), holes (h^+), and superoxide radicals ($\cdot O_2^-$) are often generated during photocatalysis and contribute to pollutant degradation. Specific scavengers, also known as quenchers, are employed to probe the involvement of these reactive species. Isopropanol (IPA) was used to selectively capture $\cdot$OH radicals, while ethylenediaminetetraacetic acid disodium (EDTA-2Na) served as a quencher for h^+. Finally, benzoquinone (BQ) was utilized to scavenge $\cdot O_2^-$ radicals.[39]

2.8 Antimicrobial activity

The emergence of multidrug-resistant bacteria necessitates the exploration of novel antimicrobial agents. This study investigates the antibacterial potential of *EC*-pod:ZnO NPs against representative Gram-positive (*Staphylococcus aureus*) and Gram-negative (*Pseudomonas aeruginosa*) bacteria using the well-diffusion method. Standardized cultures of both bacteria were inoculated onto nutrient agar plates. After incubation, wells were created in the solidified agar and loaded with varying concentrations (*e.g.*, 10, 25, and 40 μL) of the *EC*-pod:ZnO NP solution alongside negative (sterile solvent) and positive (known effective antibiotic) controls. Following a designated incubation period (typically 16–24 hours) at 37 °C, the diameters of clear zones surrounding the wells were measured. NPs and data are statistically analyzed to determine the minimum inhibitory concentration (MIC) of the ZnO NPs against the tested bacteria. This approach facilitates a comprehensive evaluation of the dose-dependent antibacterial activity of *EC*-pod:ZnO NPs, offering insights into their potential as novel antimicrobial agents.

Note: Antibacterial activity experiments involving *S. aureus* and *P. aeruginosa* were conducted in a Biosafety Level 2 (BSL-2) facility under strict aseptic conditions. A closed glove box was used to handle live cultures. Personal Protective Equipment (PPE) was consistently used throughout the experimental procedures, including lab coats, double-layered disposable gloves, face masks, and protective eyewear. All working surfaces, instruments (*e.g.*, Petri dishes, forceps), and the interior of the glove box were thoroughly sterilized before and after use. And biohazardous waste was handled and discarded in accordance with institutional biosafety guidelines.

3 Results and discussion

3.1 XRD analysis

The XRD pattern presented in Fig. 1(a) illustrates the diffraction peaks of *EC*-pod:ZnO calcined at low temperature (80 °C). The

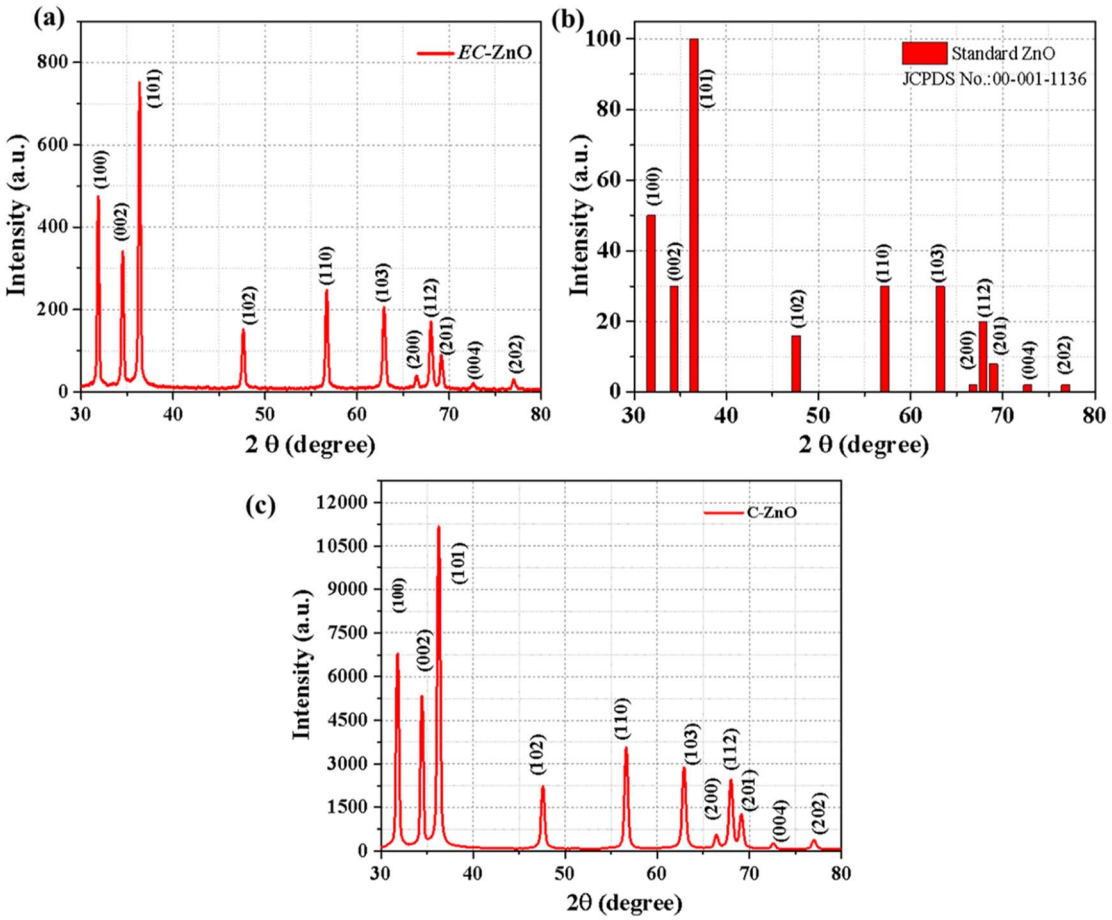

Fig. 1 (a) X-ray diffraction pattern of *EC*-pod:ZnO (at 80 °C), (b) Standard ZnO (JCPDS No. 00-001-1136), and (c) X-ray diffraction pattern of *EC*-pod:ZnO (at 400 °C).

diffraction peaks correspond to 2θ angles at 31.80°, 34.50°, 36.39°, 47.56°, 56.73°, 63.0°, 66.58°, 67.90°, 69.0°, 72.56° and 76.9° corresponding to the (100), (002), (101), (102), (110), (103), (200), (112), (201), (004) and (202) planes, respectively, and well-matched with JCPDS card No: 00-001-1136 (Fig. 1(b)). These XRD peaks align well with previous results reported for *EC*-seed extract-mediated ZnO,[26,27] which have the potential for antibacterial, larvicidal, and anticancerous activity. Thus, it confirms the developed hexagonal wurtzite phase of ZnO NPs utilizing *EC*-pod extract. Moreover, the absence of any supplementary diffraction peaks associated with impurities or defects serves as additional evidence of the purity of the *EC*-pod:ZnO NPs. The presence of narrow and well-defined sharp diffraction peaks, suggests a structure of ZnO with high crystallinity.[30] Additionally, XRD pattern of *EC*-pod:ZnO calcined at higher temperature (C-ZnO at 400 °C), is presented in Fig. 1(c). It is

Table 2 Crystallite size of *EC*-pod:ZnO

Sr. no.	Peak position (2θ) (degree)	Peak width FWHM (radian)	Lattice planes (*h k l*)	Crystallite size (*D*) (nm)	*d* (nm)
1	31.86	0.00651	(1 0 0)	23.13	2.80
2	34.52	0.00690	(0 0 2)	21.99	2.61
3	36.34	0.00676	(1 0 1)	22.56	2.46
4	47.63	0.00755	(1 0 2)	20.97	1.90
5	56.68	0.00739	(1 1 0)	22.27	1.62
6	62.9	0.00813	(1 0 3)	20.89	1.47
7	66.47	0.00939	(2 0 0)	18.45	1.40
8	68.01	0.00836	(1 1 2)	20.91	1.38
9	69.15	0.00817	(2 0 1)	21.55	1.35
10	72.60	0.01055	(0 0 4)	17.03	1.30
11	77.03	0.00934	(2 0 2)	19.83	1.23

Average value '*D*' = 20.87 nm

Table 3 Comparative analysis of crystallite size of *EC*-pod:ZnO with literature reports of green synthesized ZnO NPs

Sr. no.	Plant name	Crystallite size (nm)	Calcination temperature	Applications	Ref.
1	*Allium cepa*	57.38	500 °C	Antioxidant and antibacterial activity	41
2	*Dolichos lablab*	36	—	Photocatalytic and antibacterial activity	42
3	*Solanum nigrum*	20–30	400 °C	Antibacterial activity	43
4	*Myristica fragrans*	41.23	500 °C	Photocatalytic, antibacterial, antioxidant activity	40
5	*Nephellium lappaceum*	50.95	400 °C	Antibacterial activity	44
6	*Thyme*	35.2–69.9	150 °C	Not reported	45
7	*Lepidagathis ananthapuramensis*	28.12	500 °C	Photocatalytic activity	46
8	*EC*	20.87	80 °C	Photocatalytic and antibacterial activity	Present study

observed that the same ZnO crystalline phase is present, with no significant change in the diffraction peak positions. However, variations in the peak intensities are observed, indicating changes in crystallinity and possibly particle size. Since the desired phase is already achieved at 80 °C, and to preserve the organic components derived from the *EC*-pod, the ZnO sample calcined at 80 °C has been selected for further analysis and application.

Furthermore, the estimation of crystallite size (D) of *EC*-pod:ZnO NPs has been carried out using the full width at half-maximum (FWHM) value derived from each diffraction. Scherrer's equation utilized to calculate the 'D' value for *EC*-pod:ZnO is as follows:

$$D = K\lambda/(\beta \quad \cos \quad \theta) \tag{7}$$

Here, 'D', 'K' (=0.9), 'λ' (=0.154 nm) are crystallite-size, Scherrer's constant, and wavelength of X-ray radiation. 'β' and 'θ' are FWHM intensity of peak and diffraction peak's angle, respectively.

Table 2 depicts the crystallite size (D) and inter-planar spacing (d) values in nm for respective diffraction peaks. An average 'D' value is 20.87 nm.

In the existing body of literature, various plants, and their parts, including leaf extracts from *Cocos nucifera* and fruit extracts from *Myristica fragrans*, have been reported for their potential to facilitate the synthesis of ZnO NPs with a hexagonal wurtzite structure. Notably, these studies have reported comparable crystallite sizes, such as 16.6 nm and 41.23 nm, and have demonstrated the utilization of such NPs in photocatalytic applications for the degradation of Methylene blue dye.[21,40] These findings underscore the potential of bioactive molecules capable of facilitating the synthesis of photocatalytic materials with tailored properties for environmental remediation applications.

However, the crystallite size of nanoparticles synthesized using various plant extracts varies significantly based on the plant type and calcination conditions. But the present study using *EC* pod extract achieved the smallest crystallite size of 20.87 nm, notably at the lowest calcination temperature of 80 °C. In comparison, other studies reported larger crystallite sizes (>20 nm) of green synthesized ZnO (Table 3) using *Allium cepa* (at 500 °C), *Myristica fragrans* (at 500 °C), *Nephellium lappaceum* (at 400 °C), *Solanum nigrum* (at 400 °C), *Thyme vulgaris*, and *Lepidagathis ananthapuramensis*.[40,41,43–46] It is well-reported that a photocatalyst with smaller size demonstrates better

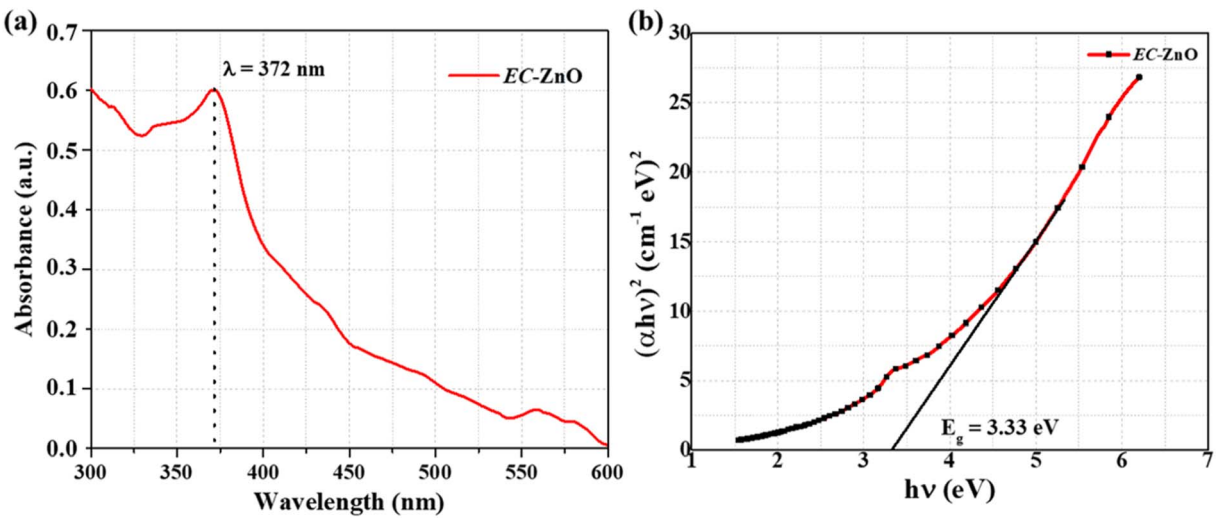

Fig. 2 (a) UV-vis spectrum and (b) Tauc plot of *EC*-pod:ZnO.

photocatalytic activity.[47,48] Thus, the combination of *EC* extract phytochemicals and a low temperature process, has resulted a fine crystallite size in the present study which indicates a more efficient synthesis route, potentially enhancing the performance of the nanoparticles.

Moreover, investigations into the bioactive components present in *EC*-pod extract have revealed their efficacy in mediating the successful synthesis of a photocatalyst featuring the anatase phase of TiO_2. This photocatalyst has shown promising potential for use in the degradation of Congo red dye.[30] Hence, it can be inferred that the current extract derived from the *EC*-pod holds significant potential as a key facilitator in the successful synthesis of a photocatalyst.

3.2 UV-vis spectrum analysis

UV-vis spectroscopy analysis conducted within the 300–600 nm wavelength range revealed a surface plasmon resonance (SPR) peak at 372 nm (Fig. 2(a)), signalling the conversion of zinc nitrate solution to ZnO NPs. This observation aligns with findings reported by Vinotha *et al.* (2020), who also noted a SPR peak at 373 nm in ZnO NPs synthesized using EC seed extract.[27] Similarly, Abdelbaky *et al.* documented a SPR peak at 370 nm for ZnO NPs synthesized utilizing leaf extract from *Cymbopogon citratus*.[49] These studies disclose that bioactive compounds present in the extract exhibit the capability to bind zinc ions, leading to the formation of complexes that upon subsequent time, decompose into ZnO.[27] And, the reduction of ZnO NPs is indicated by formed white precipitates. The corresponding band gap of *EC*-pod:ZnO is estimated by Tauc plot Fig. 2(b) which is 3.33 eV. The findings align well with the prior study of Rahman *et al.* who documented the *Cocos nucifera* leaf extract-mediated synthesis of ZnO, reporting a band gap of 3.37 eV, respectively, for photocatalytic activity.[21] It is reported in the literature that a narrower band gap is indicative of the potential for enhanced photocatalytic activity of the NPs, particularly evident in the degradation of dye.[40] This phenomenon arises from the ease with which electrons can be excited from the valence band to the conduction band due to the reduced band gap.[40] Thus, the above findings of UV-vis spectroscopy reveal that the synthesis of ZnO NPs is accomplished by utilizing *EC*-pod extract for photocatalytic activity.

3.3 FTIR spectrum analysis

The phytochemicals responsible for capping and stabilizing the formation of *EC*-pod:ZnO NPs, were inspected *via* FTIR spectra (Fig. 3). The FTIR spectrum of zinc nitrate hexahydrate

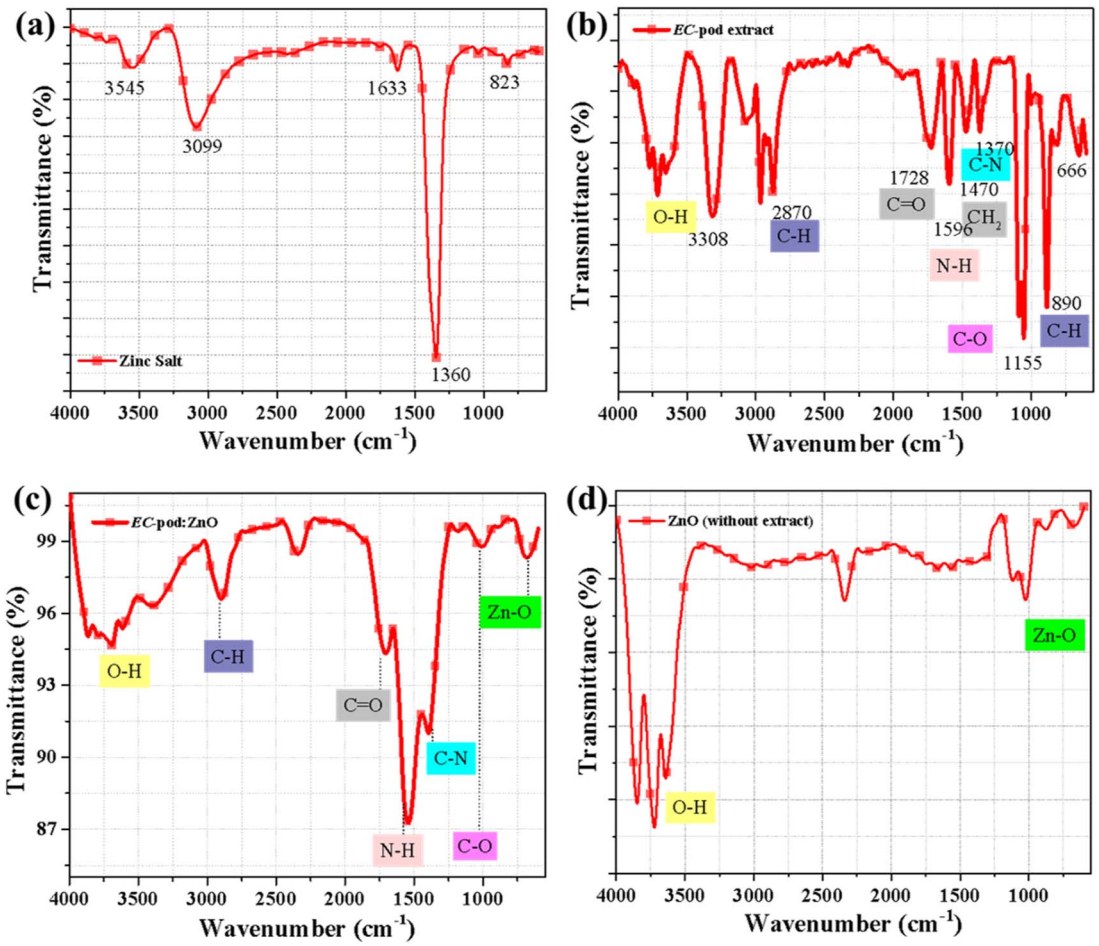

Fig. 3 FTIR spectra: (a) zinc hexanitrate dehydrate, (b) *EC* extract, (c) *EC*-pod:ZnO, and (d) ZnO (without extract).

precursor (Fig. 3(a)) depicts the bands at 823 cm^{-1}, 1360 cm^{-1}, 1633 cm^{-1}, 3099 cm^{-1}, and 3545 cm^{-1} which are consistent with previous literature report.[50] The peaks at 823 cm^{-1} and 1360 cm^{-1} correspond to the vibrational modes of the nitrate (NO_3^-) ions and peak at 3545 cm^{-1} corresponds to O–H groups. A characteristic peak observed at 832 cm^{-1} is indicative of the Zn–N bond, elucidating the coordination between zinc and nitrate groups.[51] On the other hand, Fig. 3(b) depicts the various groups of phytochemicals present in *EC*-pod extract. The peak at 2870 cm^{-1} corresponds to the stretching vibration of C–H bonds in aliphatic hydrocarbons, such as in fatty acids or other aliphatic compounds. The presence of carbonyl groups (C═O) in the extract, which could be indicative of esters, aldehydes, or carboxylic acids, is confirmed by a peak at 1728 cm^{-1}. The amide II band in the FTIR spectrum typically appears in the region of 1500–1600 cm^{-1} and is associated with bending vibrations of N–H bonds coupled with C–N stretching vibrations in proteins and peptides.[52] This band provides information about the secondary structure of proteins and is particularly sensitive to changes in hydrogen bonding and conformational changes. Therefore, the presence of the amide II band in this region suggests the presence of proteins or peptides in *EC*-pod:ZnO. Typically, a peak associated with the presence of aromatic compounds CH_2 bending vibrations in aliphatic hydrocarbons or possibly CH_3 bending vibrations is at 1470 cm^{-1}. A peak at 1155 cm^{-1} suggests the C–O stretching vibrations, which are commonly found in alcohols, phenols, ethers, or other oxygen-containing functional groups.[30]

In Fig. 3(c), the fingerprint region signifies Zn–O stretching (750–650 cm^{-1}), corroborating the presence of ZnO and metal-oxide vibrational bands.[26] Distinct band intensities of *EC*-pod:ZnO are discerned across various regions of the spectrum. An influential band at 4000–3500 cm^{-1} signifies the presence of O–H stretching of phenolic compounds, while the band at 1364 cm^{-1} indicates C–N stretching amine groups.[27] The band in region 3376–3300 cm^{-1} denotes the linking of amino acid and atmospheric CO_2.[53]. The peak at 1722 cm^{-1} is attributed to flavonoids (carbonyl group; C═O), while peaks at 1150 cm^{-1} and 1590 cm^{-1} correspond to C–O and N–H vibrations in amides-I and II linkages of proteins, respectively, and it is also depicted in extract spectrum. In literature, flavonoids have been reported to act as reducing agents during nanoparticle synthesis,[26] while proteins present in extracts exhibit capping properties.[54] Additionally, FTIR spectrum of ZnO NPs synthesized under identical reaction-conditions and parameters but in the absence of pod extract, was obtained for comparison with *EC*-pod:ZnO. FTIR spectrum of ZnO (without using extract) in displayed in Fig. 3(d) which shows peaks in the higher wavenumber region (around 4000–3500 cm^{-1}) and lower region around (1140–1028 cm^{-1} and 740–617 cm^{-1}) corresponding to the stretching and bending vibrations of –OH groups and stretching vibrations Zn–O bond, respectively.[55] No major peaks are identified in the middle region (around 1843–1234 cm^{-1}) but they are observed in *EC*-pod:ZnO due to the presence of phytochemicals of extract. Thus, above FTIR analysis confirms the successful formation of ZnO, facilitated by the

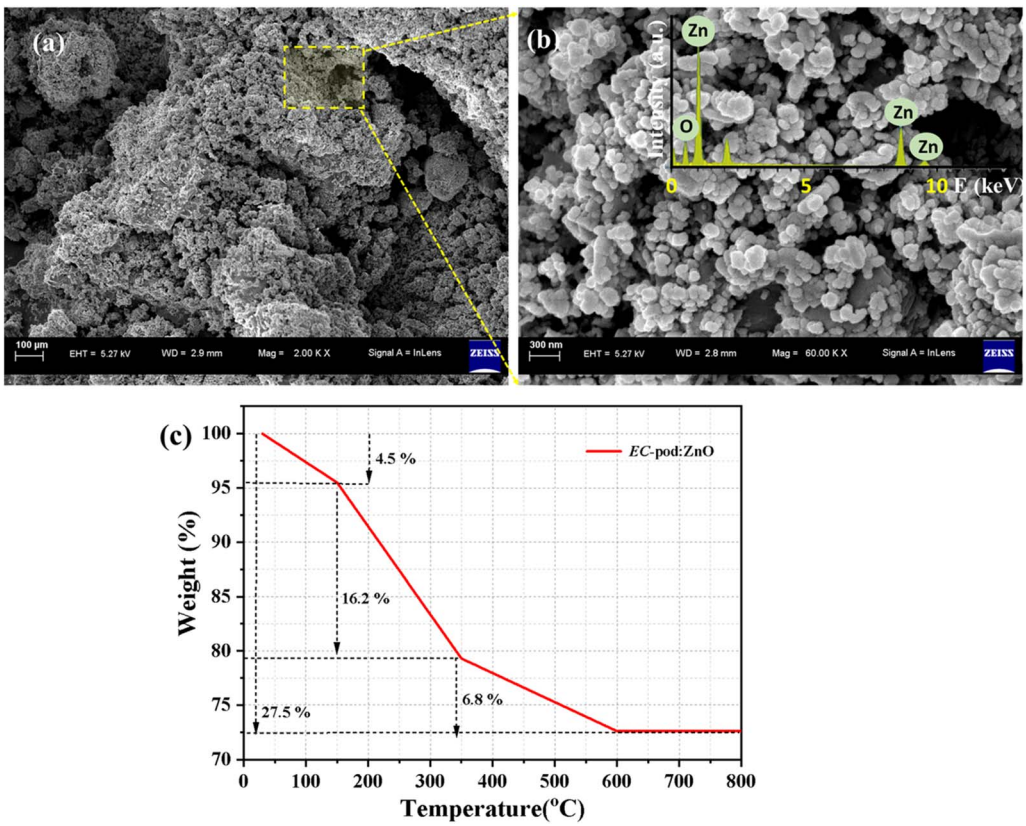

Fig. 4 FESEM micrographs (a) & (b), EDX spectrum (inset, b), and TGA of *EC*-pod:ZnO (c).

phytochemical constituents of *EC*-pod extract, which act as both reducing and capping agents, thereby contributing to the capping of NPs.

3.4 FESEM micrographs analysis

Field emission scanning electron microscopy (FESEM) serves as an indispensable tool for probing the intricate morphology of synthesized ZnO NPs. The FESEM image (Fig. 4), presented in this study offers a comprehensive analysis platform, revealing ZnO NPs at varying magnifications, thus enabling scrutiny of both particle clustering (agglomeration) and individual particle characteristics. At lower magnifications (Fig. 4(a)), the image affords a panoramic view conducive to evaluating agglomeration tendencies. Denser regions within this field suggest the presence of larger agglomerates, indicative of pronounced clustering, whereas sparser areas may denote less clustered or individual particles. On the other hand, higher magnification zones enable a more detailed examination of individual particles (Fig. 4(b)). Analysis of their outlines provides insights into their shapes; smooth and continuous outlines imply more regular geometries, such as spheres, whereas irregular outlines with sharp edges or gaps suggest less symmetrical shapes like rods or flakes. The impact of various plant extracts on ZnO nanoparticle morphology has garnered significant attention in recent literature.[56] In the context of *EC* extract, studies by Vinotha *et al.* and Pal *et al.* have shed light on its potential as a capping agent in ZnO nanoparticle synthesis.[26,27] Vinotha *et al.* demonstrated the influence of *EC* seed extract on the spherical morphology of ZnO NPs for antibacterial activity.[27] Pal *et al.*, explored that *EC* seed extract is rich in flavonoids which are reported for reducing properties.[26]

The inset of Fig. 4(b) represents an energy-dispersive X-ray spectroscopy (EDX) pattern, a crucial technique for elemental analysis in FESEM. In the context of ZnO NPs, EDX analysis offers valuable insights into their elemental composition, particularly the ratio of zinc (Zn) to oxygen (O). Achieving the optimal Zn/O ratio is fundamental for optimizing the photocatalytic performance of ZnO. While the stoichiometric ratio of ZnO is 1 : 1, deviations from this ratio can significantly impact photocatalytic activity. For instance, a controlled zinc deficiency (excess Zn) can introduce oxygen vacancies, acting as electron traps and potentially enhancing photocatalytic efficiency. Conversely, an oxygen deficiency (excess O) may introduce recombination centers, diminishing photocatalytic performance. Understanding the nuanced effects of Zn/O ratio variations requires consideration of multiple factors, including synthesis methodologies, the presence of dopants or surface modifications, and the specific photocatalytic reaction targeted. Experimental exploration is often necessary to determine the optimal Zn/O ratio tailored to a particular application. In EDX spectrum (Fig. 4(b) inset), the observed peaks of Zn (at 1 keV, 8.6 keV, and 9.5 keV) and O (at 0.5 keV) are labelled. Whereas, a small peak observed around 2.1 keV in the EDX spectrum corresponds to the M_α emission line of gold. This signal arises due to the thin gold (Au) coating applied to the *EC*-pod:ZnO sample during preparation for FESEM-EDX analysis for better imaging resolution. Although the Au coating is very thin, its characteristic peak is detectable in the EDX spectrum. It is a common and expected peak in EDX analysis of non-conductive materials, and it does not interfere with the primary interpretation of the Zn and O peaks associated with the *EC*-pod:ZnO. Moreover, the first small peak observed around 0.27 keV corresponds to carbon (C), which is originated from the organic phytochemicals present in the *EC* pod extract. Thus, presence of carbon confirms the successful involvement of the *EC* extract in the formation of nanoparticles and their surface modification process. However, the intensity of the carbon peak is significantly lower than that of Zn and O, indicating that the ZnO dominates the composition of the nanomaterial. On the other hand, the peak (at 0.52 keV) representing the total O content in the sample, includes contributions from both the ZnO lattice and the oxygen-containing functional groups of the *EC* pod extract. The observed weight percentage values for Zn, O, C, and Au are 52.80%, 20.94%, 8.0% and 18.26% while atomic percentage values are 28.09%, 45.52%, 23.17%, and 3.22, respectively. These values show that Zn and O together constitute the major component in terms of weight, confirming the presence of ZnO. Comparable elemental peaks of Zn, O, C, and Au have also been reported in a previous study involving *Salvia hispanica* mediated ZnO NPs, which were evaluated for their antibacterial properties.[57] In that study, the ZnO sample exhibiting higher antibacterial efficacy compared to other samples showed a Zn, O, and Au weight percentage of 59.41%, 19.45%, and 21.14%, respectively. During EDX analysis of ZnO NPs, the absence of any other additional peaks signifies the purity of the sample, indicating minimal impurities or dopant elements present.

3.5 TGA analysis

To quantify the ZnO content in the *EC*-pod:ZnO, TGA was performed under nitrogen atmosphere. The TGA plot shown in Fig. 4(c) illustrates the thermal stability of *EC*-pod:ZnO NP. The TG-curve reveals a total weight loss of approximately 27.5% up to 600 °C, indicating the progressive removal of volatile and organic constituents. An initial weight loss of about 4.5% occurs up to 160 °C, attributed to the evaporation of adsorbed water molecules and residual moisture from the surface of the particles. This is followed by a significant weight loss of around 16.2% between 160 °C and 340 °C and 6.8% from 340 °C to 600 °C, which can be ascribed to the thermal decomposition of bio-organic compounds present in the *EC* extract that served as reducing and capping agents during synthesis. Notably, above 600 °C, no substantial weight loss is observed. These observations are consistent with previous studies on green synthesized ZnO NPs which have been reported for 42.51% weight loss upto 600 °C.[58] Thus, the residual weight of ~72.5% confirms the dominant presence of ZnO as the thermally stable metal oxide NPs.

3.6 HRTEM analysis

To validate the formation of *EC*-pod mediated ZnO NPs, TEM and HRTEM examination was conducted by obtaining

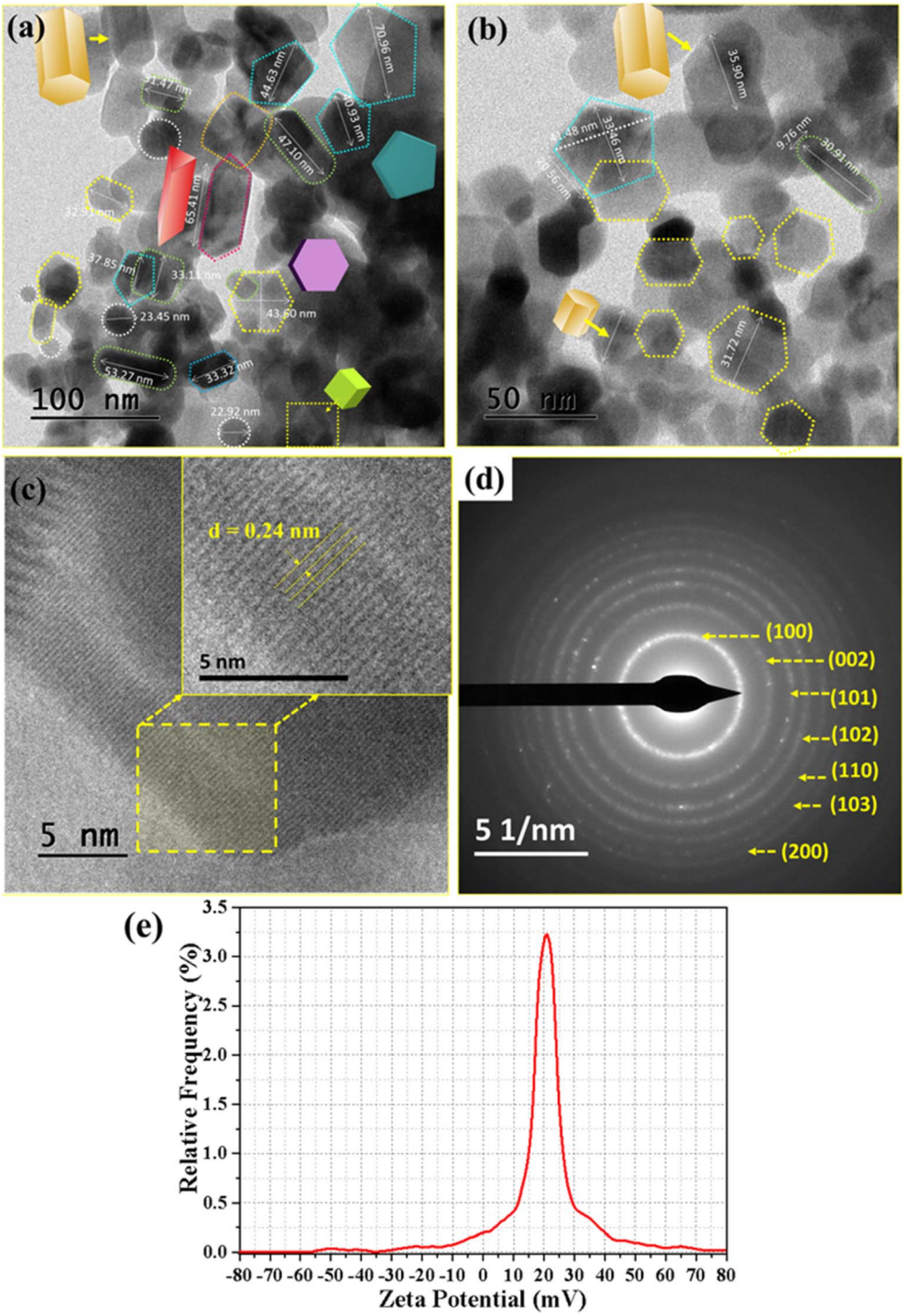

Fig. 5 (a and b) TEM images, (c) HRTEM image, (d) SAED pattern, and (e) zeta potential of *EC*-pod:ZnO.

micrographs (Fig. 5). Fig. 5(a and b) exhibiting the morphology features of *EC*-pod:ZnO showcase the dispersion of multi-structured particles with slight aggregation. The bar scale reveals that particles are in the nano-dimension range (below 100 nm). Interestingly, NPs of various shapes including pentagons, hexagons, spheres, capsule/rod-like, hexagonal-prism, triangular-prism, and cubes, all of which possess nano-scale dimensions. Line drawing models to illustrate these obtained shapes have been drawn and included in Fig. 5(a and b). It is evident that while some hexagons exhibit well-defined shapes, others appear slightly elongated (Fig. 5(a and b)). Additionally, fully developed pentagons are discernible in various orientations, with height ranging approximately from 37 nm to 71 nm. Capsule and hexagonal-prism-like structures are observed to exceed a length of 30 nm. Detailed measurements of one of the pentagons, including its height, side length, and vertex-to-

vertex distance, are conducted, all of which are found to be within the nanometre scale.

HR-TEM micrograph (Fig. 5(c)) provides further insight, revealing clear lattice fringes of *EC*-pod:ZnO NPs. For closer examination, a region '*R*' (marked in Fig. 5(c)) has been considered at higher magnification unveiling well-resolved lattice fringes (inset of Fig. 5(c)). This magnified region exhibits an interplanar spacing of 0.24 nm, attributing to the (1 0 1) crystal plane of ZnO.[37] Furthermore, the selected area electron diffraction (SAED) pattern (Fig. 5(d)) demonstrates distinct rings with bright spots, affirming the crystalline nature of *EC*-pod:ZnO NPs.[27]

The above-mentioned findings reveal the diverse morphologies in the present synthesis process, suggesting a potential role of the *EC*-pod extract in modulating the growth kinetics of ZnO NPs. Bioactive molecules of plant extract can adsorb onto the surface of growing ZnO NPs, selectively affecting different crystal faces and influencing growth rates. These bio-molecules can also act as capping agents, preventing uncontrolled growth and stabilizing the NPs. This leads to the formation of various morphologies.[30] It is noteworthy that specific morphologies exert a profound influence on the properties of NPs, consequently shaping their applicability across diverse domains. Literature reports have demonstrated that various shapes could be obtained by different plant extracts and are advantageous for photocatalytic applications.[59,60] Moreover, it have been reported spherical and rectangular-cuboid structures for the photodegradation of Congo red dye by utilizing a similar *EC*-pod extract for the synthesis of TiO_2 photocatalyst.[30] Thus, *EC*-pod extract-derived structures would hold promise as potential photocatalysts.

3.7 Zeta potential of *EC*-pod:ZnO

Zeta potential depicts the surface charge of nanoparticles (Fig. 5(e)) and serves as a key indicator of colloidal stability. As shown in Fig. 5(e), *EC*-pod:ZnO NPs exhibit a positive zeta potential with average value of 20.5 ± 0.4 mV. It indicates surface protonation and strong electrostatic repulsion. Such repulsion prevents particle aggregation which in turn maintains stable dispersion. Previous studies on green synthesized ZnO NPs exhibiting zeta values of −22.1 mV, −7.45 mV, 11 mV, and 33.1 mV have also been reported for biological and environmental applications.[40,61–63] Literature suggests that dispersions with zeta potentials above +30 mV and lower than −30 mV are highly stable, while values between ±20–30 mV ensure moderate stability.[40,64] This stability not only prevents aggregation but also promotes better surface accessibility, which further improves adsorption efficiency. This surface charge behavior is critical in tailoring the ZnO NPs performance in applications such as photocatalysis and antibacterial activity, where pH-dependent interactions influence performance outcomes.

Although adsorption between positively charged *EC*-pod:ZnO NPs and cationic MG dye can affect due to electrostatic interactions. But, a similar study suggests that effective dye degradation can still occur[61] due to other factors like hydrogen bonding, dipole interactions, and van der Waals forces. Moreover, variations in pH due to dispersion of *EC*-pod:ZnO in dye solution, can alter surface charge properties, influencing the overall adsorption and photocatalytic behavior.

3.8 Proposed mechanism of formation of diverse nanostructures of *EC*-pod:ZnO

When zinc solution is introduced into the *EC*:pod extract containing phytochemicals, the reduction of zinc ions (Zn^{2+} to Zn^{0+}) and stabilization of nanoparticles begins. During this synthesis process, the formation of precipitates is indicated by a color change (light yellow to white) and a decrease in pH due to the presence of acidic phytochemicals in the plant extract, such as polyphenols and organic acids (as evidenced by FTIR). The pH typically decreases as the reduction process progresses and protons are released during synthesis. This change indicates the involvement of acidic groups such as –OH and –COOH from the extract in the reaction.[65] These –OH groups, derived from phenols in the extract (as indicated by FTIR analysis), interact with zinc ions, facilitating their reduction to metallic zinc ($Zn^{2+} \rightarrow Zn^{0}$). Literature also confirms that phenolic content containing –OH groups serve as reducing agents for metal ions.[34]

The reduction of zinc ions leads to the formation of zinc hydroxide, which eventually transforms into solid ZnO NPs. Once the solid NPs are formed, the phytochemicals in the *EC* extract function as capping agents. These phytochemicals can include flavonoids, tannins, terpenoids, saponins, alkaloids, and coumarins feature functional groups such as –OH, C–N, N–O, C=O, C–O, and C=C.[34,65] These functional groups, containing electronegative oxygen and nitrogen atoms, exhibit a strong affinity for the metal oxide surface. Among the above-mentioned groups, the presence of C=O, N–H, and C–N groups are specifically identified as capping ligands (FTIR). Through selective binding, these groups influence the particles' shape, size, and growth by minimizing agglomeration. Thus, the presence of these functional groups has facilitated the formation of non-spherical ZnO NPs with distinct morphologies (FESEM, HRTEM). The diversity of shapes is attributed to the variability in functional groups, their composition and binding mechanisms, which stabilize specific crystallographic planes, promoting directional growth and patterns. The orientation of functional groups also influences the growth directions and shape of the NPs, leading to unique anisotropic structures. For example, C=O, C–O, and C=C groups are identified as capping ligands that guide the anisotropic growth of particles, resulting to non-spherical morphologies.[66] Also, similar trend has been found in the literature reports which suggest that acidic medium can lead to slower nucleation and growth, resulting in larger or more anisotropic structures.[34,67] And, it is well supported by the zeta potential results. While alkaline conditions often promote fast nucleation, smaller and more homogeneously distributed spherical nanoparticles.

Further, the absence of aggregation, possibly due to reduced van der Waals interactions and fewer surface –OH groups, ensures that the nanocrystals remain well-dispersed and can self-assemble into organized structures.[66] This organized assembly is facilitated by the ability of the particles to rotate

freely, unhindered by agglomeration. It has been reported that higher extract concentration enhances the kinetics of nanoparticle formation and control the particle's growth whereas excessive extract may lead to agglomeration due to overcapping.[34]

Ultimately, the combination of controlled reduction, selective capping, and precise growth mechanisms results in multi-structured ZnO NPs with high crystallinity, as confirmed by FESEM, TEM, and XRD analysis. In achieving crystalline and well-developed phase of material, reaction time plays a key role. Insufficient reaction time can result in incomplete formation or non-uniform particles. On the other hand, longer reaction times allow for the complete reduction of metal precursors and crystal growth, which may lead to changes in morphology such as increased size or transition from amorphous to crystalline forms.[68]

The proposed reaction mechanism illustrating the formation of ZnO NPs mediated by *EC* extract is as follow:

$$Zn_{(\text{from zinc salt})}^{2+} + EC\text{:pod extract}_{(\text{compound})} \rightarrow (Zn/EC\text{:pod extract}_{(\text{compound})})^{2+} \quad (8)$$

$$(Zn/EC\text{:pod extract}_{(\text{compound})})^{2+} + H_2O \rightarrow Zn(OH)_2 + (2H\text{-}EC\text{:pod extract}_{(\text{compound})}) \quad (9)$$

$$Zn(OH)_2 + (2H\text{-}EC\text{:pod extract}_{(\text{compound})}) + \text{heat} \rightarrow ZnO_{(\text{different nanostructures})} + (2H\text{-}EC\text{:pod extract}_{(\text{compound})}) \quad (10)$$

Thus, in the present study, the formation of various ZnO structures (pentagons, hexagons, spheres, capsule/rod-like, hexagonal-prism, triangular-prism, and cubes) using *EC*:pod extract is attributing to the presence of various phytochemicals in the *EC*:pod extract and their successful utilization in the synthesis of ZnO.

3.9 Photocatalytic activity investigation

3.9.1 UV-vis spectra and kinetic study of MG dye degradation. The investigation focused on analyzing the degradation profile of MG dye using *EC*-pod:ZnO as a photocatalyst. Initially, a controlled study was conducted without incorporating *EC*-pod:ZnO, revealing a minimal reduction in MG dye concentration over time (Fig. 6(a)). Subsequently, two concentrations of *EC*-pod:ZnO photocatalyst (10 mg and 20 mg) were tested with a fixed MG dye concentration, monitoring their effects on

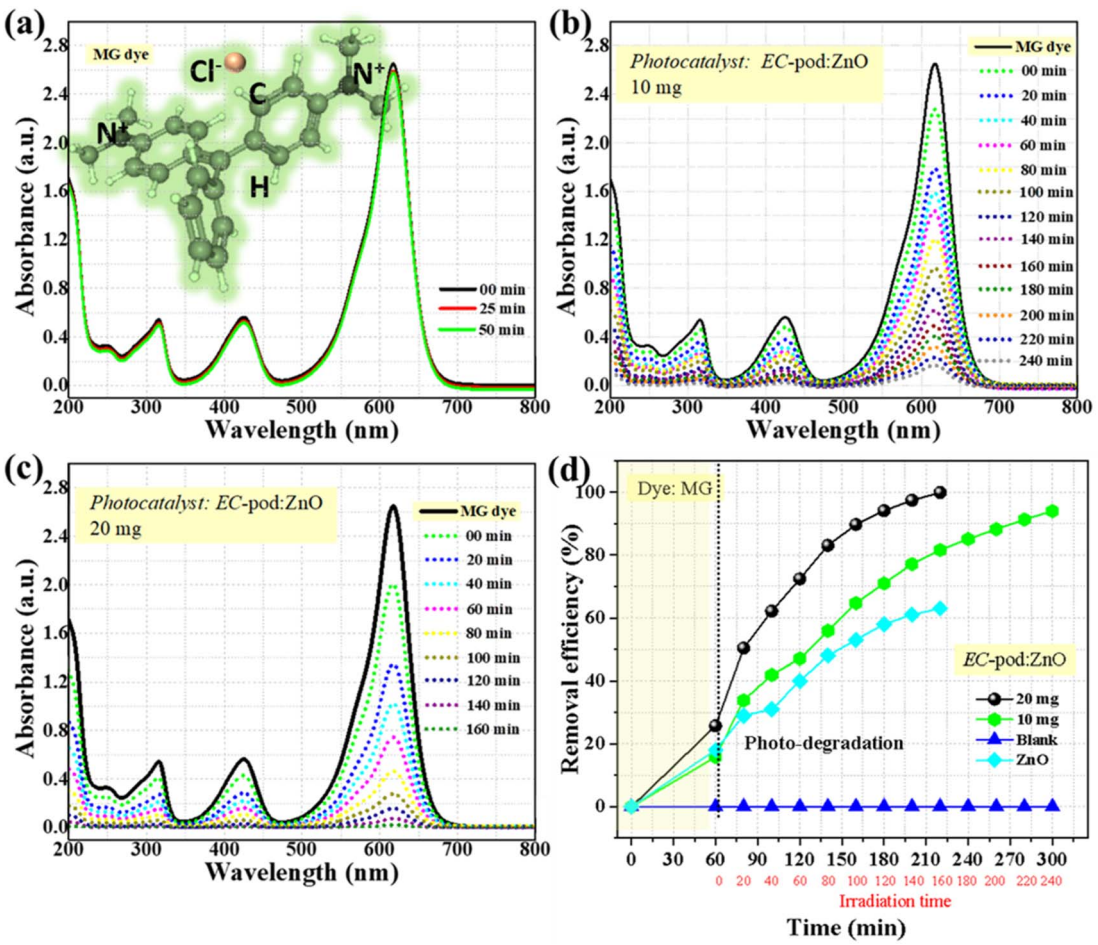

Fig. 6 Stability of MG dye; (a) without *EC*-pod:ZnO, and (b and c) with different conc. of *EC*-pod:ZnO (10 mg and 20 mg) and (d) degradation profile of MG dye using *E. cardamomum* mediated ZnO.

degradation over 240 minutes (Fig. 6(b and c)). The characteristic absorption peak of MG at 664 nm was noted to sharply diminish within the initial 60 minutes of darkness, followed by a gradual reduction throughout exposure to UV light (0–240 minutes). As expected, a higher *EC*-pod:ZnO concentration (20 mg) led to a more rapid decrease in MG dye absorbance intensity, indicating enhanced degradation with increased exposure time, achieving nearly complete degradation within 160 minutes. The percentage removal efficiency of MG dye was then estimated and plotted in Fig. 6(d).

These results demonstrate a faster degradation rate using 20 mg *EC*-pod:ZnO, with a higher percentage removal efficiency (99.8%) compared to 10 mg *EC*-pod:ZnO (Fig. 6(d)). Conversely, 10 mg *EC*-pod:ZnO degraded 94% of the MG dye over 240 minutes, while negligible removal efficiency was observed without a photocatalyst. Moreover, the photocatalytic activity of *EC*-pod:ZnO was compared with that of ZnO synthesized without extract. The comparison aimed to assess the relative efficiency of the synthesized *EC*-pod:ZnO. As shown in Fig. 6(d), *EC*-pod:ZnO exhibited the highest pollutant removal efficiency of 99.7%, significantly surpassing the ZnO, which achieved efficiency of 63% at same dose of 20 mg. This outstanding performance highlights the potential of *EC*-pod:ZnO as a superior photocatalyst, which can be attributed to its unique multi-structural and surface properties. Thus, these findings suggest the crucial role of *EC*-pod:ZnO dose in photocatalytic degradation, with higher concentrations facilitating more efficient breakdown of MG dye molecules.

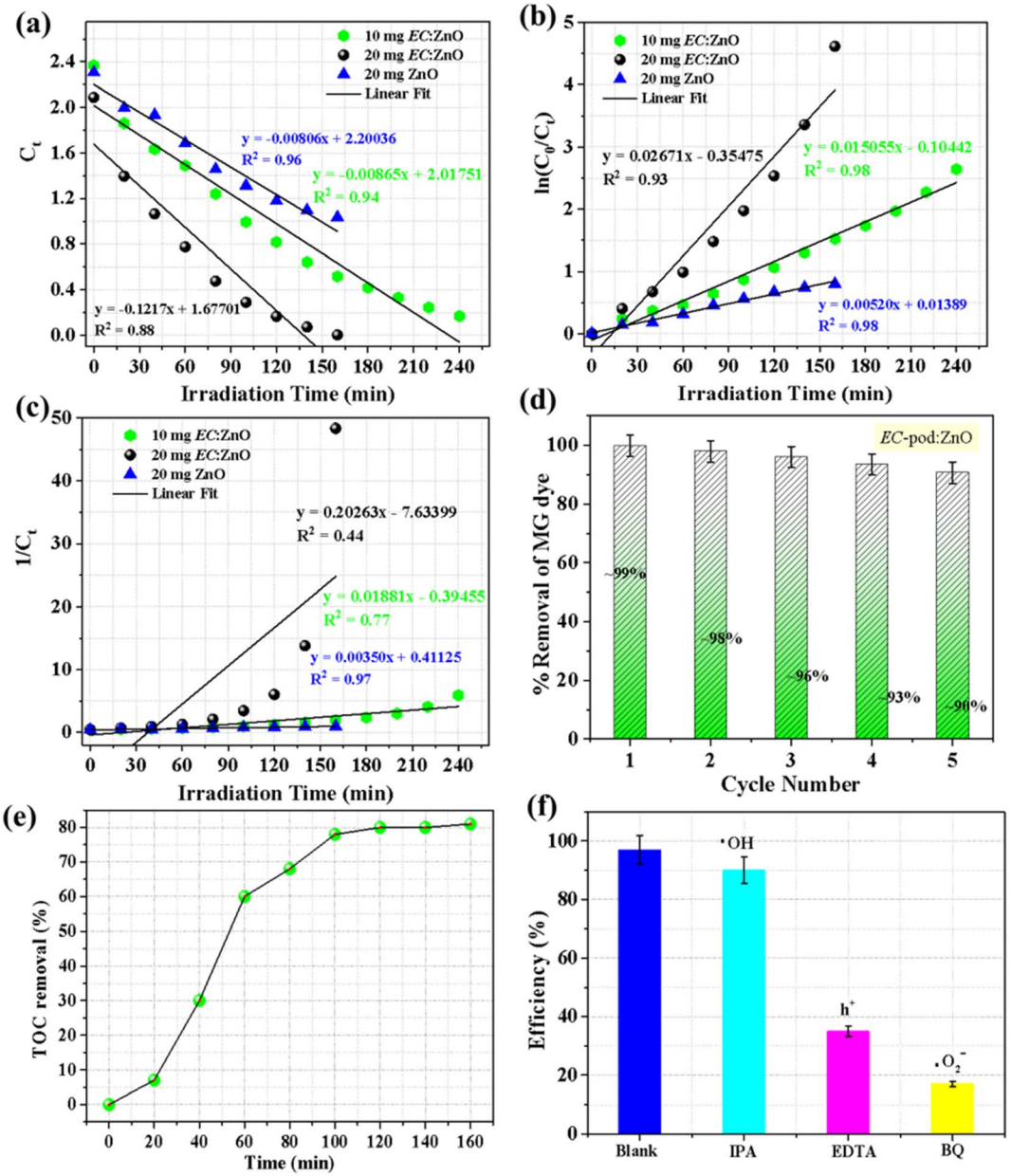

Fig. 7 (a–c) Kinetic plots of the degradation of MG dye using *EC*-pod:ZnO and ZnO (without extract), (d) Reusability, (e) TOC removal efficiency of MG dye, and (f) impact of scavengers on MG dye removal.

Additionally, the obtained data for *EC*-pod:ZnO and ZnO (without extract) were analysed using the pseudo-zero-order, first-order, and second-order kinetic models (Fig. 7(a–c)).[30,37] The fitted data plot (Fig. 7(b)) showed the best fit linear trend with a regression coefficient (R^2) value of (0.93 and 0.98), confirming first-order photocatalysis behaviour. And, the degradation reaction rate constants (k_1) of MG were calculated as 0.01505 min^{-1} and 0.02671 min^{-1} using 10 mg and 20 mg *EC*-pod:ZnO, respectively. While the k_1 value for ZnO (without extract) was 0.00520 min^{-1} for first-order kinetics.

The '*k*' value for 20 mg *EC*-pod:ZnO is found to be 1.77-fold higher than that of 10 mg *EC*-pod:ZnO and 5-fold times higher that of ZnO synthesized without the pod extract, indicating a faster reaction rate. All computed values of '*k*' and 'R^2' for models are listed in Table 4. The reusability of photocatalysts is a critical aspect in determining their practical viability. Evaluating the catalytic efficiency of *EC*-pod:ZnO NPs through multiple usage cycles provides valuable insights into their stability and effectiveness over time. As depicted in Fig. 7(d), despite a ~1% decrease in catalytic degradation of MG dye after the first cycle, the efficiency of the NPs improved with subsequent cycles, with a reduction to ~9% after the fifth cycle. This observed trend emphasizes the importance of reusability, highlighting the potential for prolonged and sustainable application of photocatalysts in wastewater treatment and environmental remediation.

To assess the extent of MG dye mineralization beyond decolorization, the TOC content of the solution was monitored during UV irradiation for up to 160 minutes. The results are presented in Fig. 7(e). In the initial 20 minutes of the photodegradation, a small increase in the percentage (~7%) of mineralization of organic species is detected. Following this, in the next 40 minutes, the mineralization process accelerates significantly, displaying a sharp increase of ~53% (total ~60% after 60 minutes of irradiation). During the subsequent 40 minutes, it continues to rise, attaining ~80%. After that, the mineralization process approaches saturation. Thus, the TOC removal reaching ~80% indicates significant mineralization of the dye into smaller organic molecules under UV irradiation in the *EC*-ZnO photocatalyst system. This observation underscores the effectiveness of UV light as a driver for MG degradation within the *EC*-ZnO photocatalytic process.

3.9.2 Photocatalytic mechanism by *EC*-pod:ZnO photocatalyst. The trapping experiment using scavengers was conducted during the photocatalytic reaction with *EC*-pod:ZnO to elucidate the reaction mechanism. As shown in Fig. 7(f), the addition of IPA, a ·OH quencher, did not significantly affect the photodegradation of MG dye. This suggests minimal involvement of ·OH radicals in the degradation process. In contrast, the addition of BQ, $\cdot O_2^-$ quencher, led to a substantial decrease in MG degradation. This indicates that $\cdot O_2^-$ plays a crucial role in the photocatalytic process. The addition of EDTA-2Na, a h^+ quencher, resulted in a slight decrease in degradation efficiency. While h^+ may contribute to some extent, the significant suppression observed with BQ suggests that $\cdot O_2^-$ is the primary oxidizing species responsible for MG degradation in the *EC*-pod:ZnO photocatalyst system.

Upon exposure to light, the *EC*-pod:ZnO photocatalyst absorbs photons, generating electron–hole pairs in the valence band (VB) and conduction band (CB), respectively.[60] The photogenerated electrons in the CB and holes in the VB are highly reactive species. These species participate in redox reactions with adsorbed water and oxygen molecules, leading to the formation of ·OH and $\cdot O_2^-$ radicals, which are powerful oxidizing agents.[60] MG dye molecules present in the aqueous solution are adsorbed onto the surface of *EC*-pod:ZnO due to electrostatic interactions and surface defects. The adsorbed MG dye molecules are then oxidized by the generated ·OH and $\cdot O_2^-$ radicals on the surface of the *EC*-pod:ZnO. This oxidation process breaks down the MG dye molecules into smaller, less harmful fragments, ultimately leading to their mineralization into CO_2 and H_2O. The entire photocatalytic mechanism is illustrated in Fig. 8, encompassing the following involved steps:[60]

(1) Photon absorption and generation of electron–hole pairs:

$$EC\text{-pod:ZnO} + h\nu \rightarrow EC\text{-pod:ZnO}^* \quad (\text{where } h\nu \text{ represents a photon of light}) \tag{11}$$

(2) Generation of reactive species:

$$EC\text{-pod:ZnO}^* + H_2O \rightarrow EC\text{-pod:ZnO} + \cdot OH + H^+ + e^- \quad (\text{hydroxyl radical generation}) \tag{12}$$

$$EC\text{-pod:ZnO}^* + O_2 \rightarrow EC\text{-pod:ZnO} + \cdot O_2^- \quad (\text{superoxide radical generation}) \tag{13}$$

(3) Adsorption of MG dye:

$$MG + EC\text{-pod:ZnO} \rightarrow MG\text{-}EC\text{-pod:ZnO} \tag{14}$$

(4) Oxidation of MG dye:

$$MG\text{-}EC\text{-pod:ZnO} + \cdot OH \rightarrow \text{degraded products} \tag{15}$$

$$MG\text{-}EC\text{-pod:ZnO} + \cdot O_2^- \rightarrow \text{degraded products} \tag{16}$$

Table 4 Kinetic parameters for the degradation of MG dye using *EC*-pod:ZnO and ZnO (control)

			Pseudo-zero-order		Pseudo-first-order		Pseudo-second-order	
Sr. no.	Material	Catalyst dose (mg L^{-1})	k_0 (mg L^{-1} min^{-1})	R^2	k_1 (min^{-1})	R^2	k_2 (L mg^{-1} min^{-1})	R^2
1	*EC*:ZnO	100	0.00865	0.94	0.01505	0.98	0.01881	0.77
2	*EC*:ZnO	200	0.12170	0.88	0.02671	0.93	0.20263	0.44
3	ZnO	200	0.00806	0.96	0.00520	0.98	0.00350	0.97

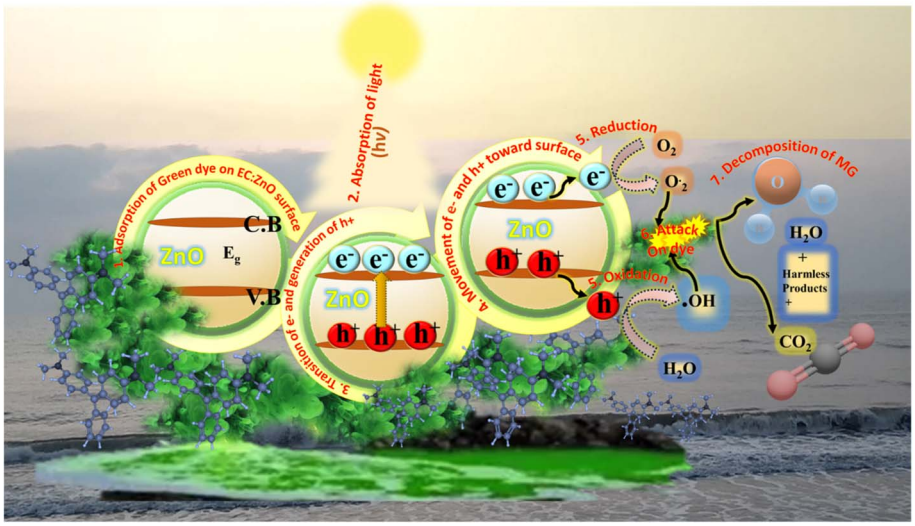

Fig. 8 Photodegradation of MG dye using *EC*-pod:ZnO.

(5) Mineralization:

$$\text{Degraded products} \rightarrow CO_2 + H_2O \quad (17)$$

3.9.3 Comparative analysis of removal efficiency. Comparison with previously reported studies in the literature regarding the removal efficiency of MG dye using ZnO NPs mediated with *EC*-pod extract is presented in Table 5. The findings indicate that the *EC*-pod:ZnO photocatalyst utilized in this investigation demonstrates notably higher removal efficiency in comparison to prior studies. For example, Sadiq *et al.* documented a removal efficiency of 91% for 20 mg of *Syzygium cumini*:ZnO photocatalyst over 180 minutes, whereas the present study achieved a substantially higher removal efficiency of 99.8% for *EC*-pod:ZnO with a 20 mg photocatalyst dose in just 160 minutes (Table 5).[69] Likewise, the present study's removal efficiency surpasses that reported by other researchers for ZnO utilizing *Azadirachta indica* (82%, 180 minutes), *Piper nigrum* (84.94%, 220 minutes), and *Punica granatum* (93%, 180 minutes).[53,71,72] Another study achieved 98% removal efficiency within 100 minutes using a fourfold higher dose of *Citrus limetta*:ZnO photocatalyst (80 mg) than that of the present *EC*-pod:ZnO (20 mg).[73] In a similar investigation by Ibarra-Cervantes *et al.*, the photodegradation efficiency of 20 mg of *Tillandsia recurvata* mediated ZnO reached 100%, but for a lesser amount of dye (10 mg) over a longer exposure duration (180 minutes) compared to the present study.[70] Moreover, compared with different types of photocatalysts such as TiO_2, FeO, SnO_2, and CuO, the present photocatalyst has superior performance with high efficiency (99.8% within 160 minutes), high quantum yield (2.73×10^{-3} molecules per photon), and space-time values (1.37×10^{-5} molecules per photon per mg) (Table 5). The comparisons highlight the efficacy of the *EC*-pod:ZnO photocatalyst developed in this study for the degradation of MG dye.

In light of above discussion, the present *EC*-based synthesis outperforms other green synthesis methods for ZnO NPs. The *EC* pod extract contains flavonoids and proteins that serve dual roles. Flavonoids, identified by the C=O peak in FTIR, act as reducing agents, while proteins function as capping agents, enhancing nanoparticle stability. This dual action of *EC* extract's phytochemicals sets it apart from other green synthesis methods using plant materials (Tables 1 and 5), which often lack such a robust combination of active constituents which act as capping and reducing agents. This unique combination promotes diverse morphologies, including pentagonal, hexagonal, spherical, rod-like, prismatic, and cubic structures unlike other plant-based synthesis, which predominantly yield spherical NPs (*e.g.*, with *A. indica*, *T. recurvata*, *P. granatum*) (Table 5). While spherical NPs offer high surface-to-volume ratios, they expose fewer high-energy facets, potentially limiting catalytic activity.[81,82] In contrast, non-spherical geometries like cubic, hexagonal and other nanostructures exposing distinct crystal facets, are highly reactive which significantly influence the anisotropic distribution of charges on the photocatalyst's surface.[83,84] For example; the irregular facets of pentagons can expose high-energy crystal planes, providing a larger number of active sites for photocatalysis. On the other hand, rod-like structures have anisotropic growth, offering direct pathways for charge transport along their length.[85] This reduces electron–hole recombination. Their elongated structure allows better light absorption and increased active surface area for pollutant interaction.[86,87] The high surface area and directional growth improve their photocatalytic performance compared to isotropic shapes like spheres.[88] Thus, as compared to previously reported spherical-shaped ZnO NPs by green methods (Tables 1 and 5), the diverse geometric and structural features in the present study make *EC*-pod:ZnO a highly stable and effective photocatalyst, as evidenced by the superior degradation of MG dye. Additionally, the *EC*-pod:ZnO photocatalyst demonstrates

Table 5 Comparison of reaction parameters, percentage-degradation, quantum yield, and space-time yield of present *EC*-pod:ZnO photocatalytic system with reported systems[a]

Sr. no.	P. C.	Poll	Synthesis method/plant	Wavelength λ (nm)	L. P. (W)	P. C. mass (g)	Poll. Sol. (L)	Poll. Conc. (g L^{-1})	M. W. of Poll. (g mol^{-1})	Time (h)	Deg. (%)	No. of moles of Poll. (moles)	No. of Poll. molecules (molecules)	No. of degraded Poll. molecules (molecules)	No. of photons generated (photons)	Q. Y. (molecules per photon)	S. T. Y. (molecules per photon per mg)	Ref.
(A) Degradation of dyes using ZnO as a photocatalyst																		
1	ZnO	MB	*S. cumini*	420	—	0.020	—	0.04	319.85	3	91	1.25×10^{-5}	7.53×10^{18}	6.85×10^{18}	—	—	—	69
2	ZnO	MB	*A. indica*	300	40	0.005	0.1	1.44	319.85	3	82.1	4.50×10^{-4}	2.71×10^{20}	2.23×10^{20}	6.52×10^{23}	3.42×10^{-4}	6.83×10^{-6}	53
3	ZnO	MB	*T. recurvata*	420	—	0.020	—	0.01	319.85	3	100	3.13×10^{-6}	1.88×10^{18}	1.88×10^{18}	—	—	—	70
4	ZnO	RY18	*P. nigrum*	250	6	0.030	0.1	0.12 0.12	906.10	3.66	94.72	1.32×10^{-5}	7.98×10^{18}	7.55×10^{18}	9.95×10^{22}	7.59×10^{-5}	2.53×10^{-6}	71
5	ZnO	CB	*P. granatum*	420	—	—	—	—	854.04	3	93	—	—	—	—	—	—	72
6	ZnO	RY18	*C. limetta*	250	6	0.080	0.1	0.12	906.10	1.66	98	1.29×10^{-5}	7.98×10^{19}	7.77×10^{18}	4.34×10^{22}	1.79×10^{-4}	2.24×10^{-6}	73
7	**ZnO**	**MG**	***E. cardamomum***	**250**	**6**	**0.020**	**0.1**	**0.12**	**364.911**	**2.66**	**99.8**	$\mathbf{3.29 \times 10^{-4}}$	$\mathbf{1.98 \times 10^{19}}$	$\mathbf{1.98 \times 10^{18}}$	$\mathbf{7.24 \times 10^{22}}$	$\mathbf{2.73 \times 10^{-3}}$	$\mathbf{1.37 \times 10^{-5}}$	**This work**
8	ZnO	MG	Algae	300	150	0.020	0.05	5×10^{-3}	364.911	1.0	92.50	6.85×10^{-7}	4.13×10^{17}	3.82×10^{17}	8.55×10^{23}	4.46×10^{-7}	2.23×10^{-8}	74
9	ZnO	MG	Chemical	254	8	0.240	0.1	0.02	364.911	4.0	86.00	5.48×10^{-6}	3.30×10^{18}	2.84×10^{18}	1.47×10^{23}	1.93×10^{-5}	8.04×10^{-8}	75
(B) Degradation of dyes using other photocatalysts																		
10	TiO_2	RG	*C. limon*	254	6	0.020	0.1	95×10^{-3}	1418.94	3.0	96.00	6.70×10^{-6}	4.03×10^{18}	3.87×10^{18}	8.28×10^{22}	4.68×10^{-5}	2.34×10^{-6}	76
11	TiO_2	RhB	Green	555	40	0.025	0.05	0.05	479.02	2.0	96.59	5.22×10^{-6}	3.14×10^{18}	3.04×10^{18}	8.04×10^{23}	3.78×10^{-6}	1.51×10^{-7}	77
	P25-TiO_2	RhB	Chemical	555	40	0.025	0.05	0.05	479.02	2	78.90	5.22×10^{-6}	3.14×10^{18}	2.48×10^{18}	8.04×10^{23}	3.09×10^{-6}	1.23×10^{-7}	
12	SnO_2	MB	*P. granatum*	420	—	0.03	0.1	48×10^{-3}	319.85	4.0	91.50	1.50×10^{-5}	9.04×10^{18}	8.27×10^{18}	—	—	—	78
13	FeO	IC	*A.indica*	254	16	0.025	0.1	99×10^{-3}	466.36	5.0	85	2.12×10^{-5}	1.28×10^{19}	1.09×10^{19}	3.68×10^{23}	2.95×10^{-5}	1.18×10^{-6}	79
				420	—	0.025	0.1	99×10^{-3}	466.36	5.0	79	2.12×10^{-5}	1.28×10^{19}	1.01×10^{19}	—	—	—	
14	CuO	CR	*S. alternifolium*	420	—	0.080	0.1	0.01	696.66	5.3	71.22	1.44×10^{-6}	8.64×10^{17}	6.16×10^{17}	—	—	—	80
						0.040					73.78	1.44×10^{-6}	8.64×10^{17}	6.38×10^{17}				
						0.020					76.61							
						0.010					79.48							

[a] P. C.: photocatalyst, Poll.: pollutant, L. P.: lamp power, Poll. Sol.: pollutant solution, Poll. conc.: pollutant concentration, M. W.: molecular weight, Deg.: degradation, Q. Y.: quantum yield, S. T. Y.: space time yield, MB: Methylene blue, RY18: Reactive yellow 18, CB: Coomassie brilliant blue, MG: Malachite green, RG: Reactive green, RhB: Rhodamine B, IC: Indigo Carmine, CR: Congo red, Ref.: Reference. *Wavelength (λ) 254 nm/420 nm has been taken for UV/visible light exposure, respectively, wherever the value of λ is not reported.

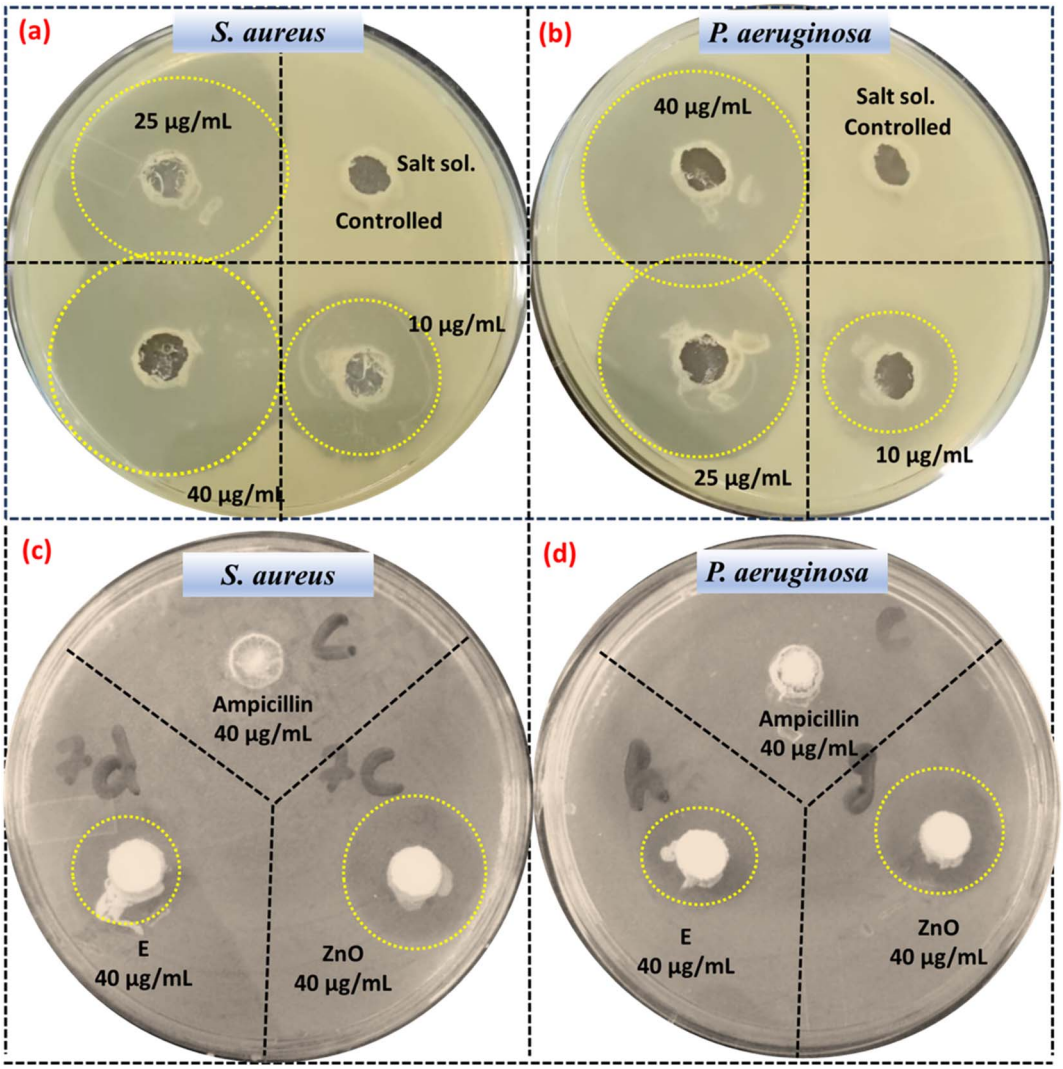

Fig. 9 Antibacterial activity against *S. aureus* and *P. aeruginosa* using: (a and b) *EC*-pod:ZnO NPs and salt and (c and d) Ampicillin, extract and ZnO synthesized without extract.

high quantum yield and space-time values, which further support its efficacy.

3.10 Evaluation of antibacterial activity

This section delineates the proposed mechanistic pathways through which *EC*-pod:ZnO NPs exert their potent antibacterial effects against *S. aureus* and *P. aeruginosa*. Fig. 9 displays the zones representing areas of bacterial growth inhibition caused by the diffusion of *EC*-pod:ZnO (Table 6). A critical factor in this interaction is the negatively charged bacterial cell wall, characteristic of both Gram-positive and Gram-negative bacteria, which facilitates the initial binding and subsequent actions of the *EC*-pod:ZnO NPs (Fig. 10). The bacterial cell wall is essential for maintaining cellular integrity, protecting against environmental stressors, and ensuring efficient nutrient uptake. Upon exposure to *EC*-pod:ZnO NPs, multiple mechanisms are postulated to contribute to bacterial cell death. The primary interaction is hypothesized to be electrostatic, where the negatively charged bacterial cell wall attracts the positively charged *EC*-

Table 6 *EC*-pod:ZnO nanoparticles' inhibition zones for *P. aeruginosa* and *S. aureus*

Sr. no.	Volume	*S. aureus* inhibition zone (cm)	*P. aeruginosa* inhibition zone (cm)	Mean inhibition zone (cm)	Standard deviation (cm)
1	10 µL	1.312	1.002	1.157	0.219203
2	25 µL	2.412	2.014	2.213	0.281428
3	40 µL	3.014	2.913	2.964	0.071418

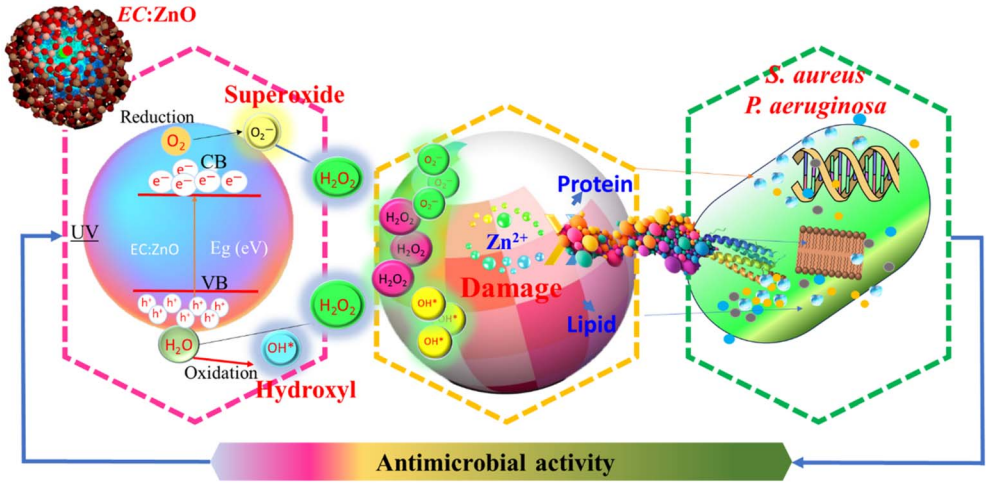

Fig. 10 Schematic of antibacterial action mechanism of *EC*-pod:ZnO NPs.

pod:ZnO NPs, initiating a series of disruptive events.[30] This interaction can compromise cell membrane integrity, leading to the leakage of vital cellular contents and disruption of critical bacterial functions.

Moreover, ZnO NPs have the capability to generate reactive oxygen species (ROS) under appropriate conditions. These ROS induce oxidative stress within bacterial cells, resulting in damage to crucial biomolecules such as proteins, lipids, and DNA, thereby culminating in cell death. The role of *EC* in mediating these effects is particularly noteworthy, as it may enhance the generation of ROS and facilitate deeper penetration of *EC*-pod:ZnO NPs into bacterial cells. Additionally, *EC*-pod:ZnO NPs may penetrate the bacterial cell and interact with intracellular components, exacerbating their antibacterial effects. The size, concentration, and surface properties of the *EC*-pod:ZnO NPs are pivotal in determining their antibacterial efficacy, underscoring the necessity of optimizing these parameters for targeted applications.

As shown in Table 6, *EC*-pod:ZnO NPs exhibited dose-dependent antibacterial activity against both *S. aureus* and *P. aeruginosa*. The diameter of the inhibition zones surrounding the wells containing *EC*-pod:ZnO NPs increased with increasing concentration, indicating a stronger inhibitory effect at higher doses. Notably, *S. aureus* appeared to be slightly more susceptible to the NPs compared to *P. aeruginosa*, as evidenced by larger inhibition zone diameters.

In addition to these mechanistic insights, empirical evidence further supports the antibacterial potential of *EC*-pod:ZnO NPs. Table 6 illustrates the inhibition zones of ZnO NPs for *P. aeruginosa* and *S. aureus* at different concentrations of EC. For *S. aureus*, inhibition zones were observed to be 1.312 cm, 2.412 cm, and 3.014 cm for 10 μL, 25 μL, and 40 μL, respectively. Similarly, for *P. aeruginosa*, the inhibition zones measured were 1.002 cm, 2.014 cm, and 2.913 cm for the same respective volumes. These results indicate a dose-dependent increase in antibacterial activity, highlighting the efficacy of *EC*-pod:ZnO NPs against both Gram-positive and Gram-negative bacteria. In addition, control experiments were conducted using 40 μL concentration of *EC* (E) extract, ZnO (synthesized without using extract), and antibiotic (Ampicillin) (Fig. 9(c–d)). It can be seen that there is no ZOI around the wells with one test agent (Ampicillin) that indicates resistant bacterial strain to the test agent. These results are well consistent with literature report which has shown that *S. aureus* exhibits resistance to Ampicillin and Ciprofloxacin antibiotics at concentration 50 μL.[89] Thus, in the present study, *EC*-pod:ZnO (at 40 μL) is an effective antibacterial agent as compared to Ampicillin antibiotic. While other test agents such as *EC* (ZOI = 0.6 cm for both strains) and ZnO (ZOI = 1.2 cm and 0.9 cm for *S. aureus* and *P. aeruginosa*, respectively) showed some smaller ZOI as compared to *EC*-pod:ZnO NPs. Herein, the smaller ZOI observed in the control experiment with ZnO does not imply that this test agent is ineffective. It can be possible that it shows small ZOI only against the tested bacterial strains or due to incubation time. In the previous studies, some extracts didn't display ZOI but *EC* extract has been reported for showing ZOI and it exhibited antibacterial action.[63,90]

To provide statistical support for these observations, the mean inhibition zones were calculated as 1.157 cm, 2.213 cm, and 2.964 cm for 10 μL, 25 μL, and 40 μL, respectively. The standard deviations were 0.219 cm, 0.281 cm, and 0.071 cm for the respective volumes, indicating consistent antibacterial effects across different concentrations. Paired *t*-tests were performed to compare the inhibition zones at different volumes. The *t*-test between 10 μL and 25 μL showed a significant difference ($p = 0.0265$), indicating a substantial increase in antibacterial activity. Similarly, the *t*-test between 10 μL and 40 μL also showed a significant difference ($p = 0.0368$), reinforcing the dose-dependent efficacy. However, the *t*-test between 25 μL and 40 μL did not show a significant difference ($p = 0.1244$), suggesting that the antibacterial activity may reach a plateau at higher concentrations.

Thus, the antibacterial activity of *EC*-pod:ZnO NPs likely involves a multifaceted mechanism that includes membrane disruption, ROS generation, and intracellular interactions. These combined effects result in the effective inhibition and

destruction of bacterial cells. Future research should focus on elucidating the precise molecular pathways involved and optimizing the physicochemical properties of *EC*-pod:ZnO NPs to maximize their antibacterial potential. This approach will pave the way for the development of highly effective antibacterial agents tailored to combat specific bacterial pathogens. Moreover, future studies can be directed towards comprehensive cytotoxicity and biocompatibility evaluations of *EC*-pod:ZnO NPs on human cell lines, which will further provide critical insights into their safe and effective use in biomedical applications.

4 Conclusion

This study presents a novel approach for the one-pot synthesis of ZnO NPs using *E. cardamomum*-pod extract. Through various characterization techniques, including XRD, UV-Vis, FTIR, FESEM, EDX, Zeta and HRTEM, the successful synthesis of crystalline *EC*-pod:ZnO NPs is confirmed with diverse and well-defined nano-structures *i.e.*, pentagons, hexagons, spheres, capsule/rod-like, hexagonal-prism, triangular-prism, and cubes. Zeta analysis reveals the positive surface charge on *EC*-pod:ZnO NPs. The current findings also highlight the presence of C–N, N–H, C═O, and C–O groups of proteins, peptides, carboxylic acids, and phenols and their role as capping and reducing agents, in the synthesis of *EC*-pod:ZnO and as stabilizing agents for the surface of ZnO. Notably, the *EC*-pod:ZnO NPs exhibit good photocatalytic activity (99.8%) in the degradation of MG dye under UV light exposure (160 minutes), coupled with high reusability properties. The *EC*-pod:ZnO exhibits an efficient photocatalytic proficiency with its high QY measured at 2.73×10^{-3} molecules per photon, in the degradation of MG dye. Furthermore, the photocatalyst's performance is highlighted by a notable STY value of 1.37×10^{-5} molecules per photon per mg, reflecting its maximum efficiency in converting photon energy into chemical transformations per unit time and reactor volume. Furthermore, *EC*-pod:ZnO NPs have been evaluated for their antibacterial properties and demonstrate effectiveness against the bacterial strains *S. aureus* and *P. aeruginosa*. These results support the potential of *EC*-pod:ZnO NPs as useful photocatalysts for addressing environmental challenges associated with dye pollution and combating bacterial contamination.

Data availability

Data is available on request from the authors.

Author contributions

Harpreet Kaur: conceptualization, methodology, formal analysis and investigation, visualization, writing – original draft preparation, data curation, software, funding acquisition, supervision; Abhishek Sharma: methodology, writing – original draft preparation; Krishna Anand: methodology, investigation; Ankush Panday: methodology; Shavan Tagotra: methodology; Sachin Kakran: methodology; Anuj Kumar Singh: methodology; Mir Waqas Alam: review and editing; Sanjeev Kumar: supervision, project administrator; Gassoumi Bouzid: review and editing; Jasvir Dalal: formal analysis, resources and review and editing; Gurjinder Singh: review and editing.

Conflicts of interest

The authors declare that they have no known competing financial interests or personal relationships that could have appeared to influence the work reported in this paper.

Acknowledgements

The authors gratefully acknowledge Chandigarh University, Gharuan-Mohali, Punjab (India) for research lab facilities.

References

1 B. Lellis, C. Z. Fávaro-Polonio, J. A. Pamphile and J. C. Polonio, Effects of textile dyes on health and the environment and bioremediation potential of living organisms, *Biotechnol. Res. Innov.*, 2019, **3**(2), 275–290.
2 A. K. Shimi, C. Parvathiraj, S. Kumari, J. Dalal, V. Kumar, S. M. Wabaidur and Z. A. Alothman, Green synthesis of SrO nanoparticles using leaf extract of Albizia julibrissin and its recyclable photocatalytic activity: An eco-friendly approach for treatment of industrial wastewater, *Environ. Sci.:Adv.*, 2022, **1**(5), 849–861.
3 *Nanomaterials: Synthesis and Applications*, ed. J. Dalal, A. Gupta, S. Korpal and V. N. Thakur, Cambridge Scholars Publishing, 2024.
4 A. Kaur, S. Kumar, H. Kaur, G. S. Lotey, P. P. Singh, G. Singh, S. Kumar, J. Dalal, G. Bouzid, M. Misra and R. Pandey, Enhanced photocatalytic degradation and antimicrobial activities of biogenic Co3O4 nanoparticles mediated by fenugreek: sustainable strategies, *Mater. Adv.*, 2024, **5**(20), 8111–8131.
5 S. F. Ahmed, M. Mofijur, S. Nuzhat, A. T. Chowdhury, N. Rafa, M. A. Uddin, *et al.*, Recent developments in physical, biological, chemical, and hybrid treatment techniques for removing emerging contaminants from wastewater, *J. Hazard. Mater.*, 2021, **416**, 125912.
6 S. Kumari, K. Sharma, S. Korpal, J. Dalal, A. Kumar, S. Kumar and S. Duhan, A comprehensive study on photocatalysis: materials and applications, *CrystEngComm*, 2024, **26**, 4886.
7 Y. Song, L. Wang, X. Qiang, W. Gu, Z. Ma and G. Wang, The promising way to treat wastewater by microalgae: Approaches, mechanisms, applications and challenges, *J. Water Process Eng.*, 2022, **49**, 103012.
8 Y. Song, L. Wang, X. Qiang, W. Gu, Z. Ma and G. Wang, An overview of biological mechanisms and strategies for treating wastewater from printing and dyeing processes, *J. Water Process Eng.*, 2023, **55**, 104242.
9 Y. Xie, J. Hu, H. Esmaeili, D. Wang and Y. Zhou, A review study on wastewater decontamination using nanotechnology: Performance, mechanism and environmental impacts, *Powder Technol.*, 2022, **412**, 118023.

10 M. Mahajan, S. Kumar, J. Gaur, S. Kaushal, J. Dalal, G. Singh, M. Misra and D. S. Ahlawat, Green synthesis of ZnO nanoparticles using Justicia adhatoda for photocatalytic degradation of malachite green and reduction of 4-nitrophenol, *RSC Adv.*, 2025, **15**(4), 2958–2980.
11 P. Kumar, S. Kaushal, S. Kumar, J. Dalal, K. M. Batoo and D. S. Ahlawat, Recent Advancements in Pure and Doped Zinc Oxide Nanostructures for UV Photodetectors Application, *Phys. B*, 2025, **25**, 417177.
12 M. S. Chavali and M. P. Nikolova, Metal oxide nanoparticles and their applications in nanotechnology, *SN Appl. Sci.*, 2019, **1**(6), 607.
13 R. S. Brishti, M. Ahsan Habib, M. H. Ara, K. M. Rezaul Karim, M. Khairul Islam, J. Naime, *et al.*, Green synthesis of ZnO NPs using aqueous extract of Epipremnum aureum leave: Photocatalytic degradation of Congo red, *Results Chem.*, 2024, **7**, 101441.
14 M. Shahid, N. Ijaz, B. Shahid, T. Tufail, H. B. U. Ain and M. Hussain, Eucalyptus globulus Labill. Mediated synthesis of ZnO nanoparticles, their Optimization and characterization, *Cogent Food Agric.*, 2024, **10**(1), 2293332.
15 A. Zaater, M. O. Serhoud, I. Ben Amor, S. Zeghoud, A. Hemmami, A. Rebiai, *et al.*, Exploring the potential of a Ephedra alata leaf extract: Phytochemical analysis, antioxidant activity, antibacterial properties, and green synthesis of ZnO nanoparticles for photocatalytic degradation of methylene blue, *Front. Chem.*, 2024, **12**, 1367552.
16 N. A. Hussien, Antimicrobial Potential of Biosynthesized Zinc Oxide Nanoparticles Using Banana Peel and Date Seeds Extracts, *Sustainability*, 2023, **15**(11), 9048.
17 M. H. Meshkatalsadat, A. Momeni and M. R. Abdollahzadeh, Biosynthesis of Zinc Oxide Nanoparticles Using Punica granatum L. Waste Peel Extract, and Assessment of Antioxidant and Catalytic Activity, *Nano Biomed. Eng.*, 2023, **15**(4), 378–388.
18 E. Tilahun, Y. Adimasu and Y. Dessie, Biosynthesis and Optimization of ZnO Nanoparticles Using Ocimum lamifolium Leaf Extract for Electrochemical Sensor and Antibacterial Activity, *ACS Omega*, 2023, **8**(30), 27344–27354.
19 R. S. Dangana, R. C. George and F. K. Agboola, The biosynthesis of zinc oxide nanoparticles using aqueous leaf extracts of Cnidoscolus aconitifolius and their biological activities, *Green Chem. Lett. Rev.*, 2023, **16**(1), 2169591.
20 A. Sekar, P. J. Murugan and F. Paularokiadoss, Biological synthesis and characterization of zinc oxide nanoparticles (ZnONPs) from Anisomeles malabarica, *Vietnam J. Chem.*, 2022, **60**(4), 459–471.
21 F. Rahman, M. A. Majed Patwary, M. A. Bakar Siddique, M. S. Bashar, M. A. Haque, B. Akter, *et al.*, Green synthesis of zinc oxide nanoparticles using Cocos nucifera leaf extract: characterization, antimicrobial, antioxidant and photocatalytic activity, *R. Soc. Open Sci.*, 2022, **9**(11), 220858.
22 H. M. Abdelmigid, N. A. Hussien, A. A. Alyamani, M. M. Morsi, N. M. AlSufyani and H. A. Kadi, Green Synthesis of Zinc Oxide Nanoparticles Using Pomegranate Fruit Peel and Solid Coffee Grounds vs. Chemical Method of Synthesis, with Their Biocompatibility and Antibacterial Properties Investigation, *Molecules*, 2022, **27**(4), 1236.
23 A. A. Al Awadh, A. R. Shet, L. R. Patil, I. A. Shaikh, M. M. Alshahrani, R. Nadaf, *et al.*, Sustainable Synthesis and Characterization of Zinc Oxide Nanoparticles Using Raphanus sativus Extract and Its Biomedical Applications, *Crystals*, 2022, **12**(8), 1142.
24 Q. M. Thi Tran, H. A. Thi Nguyen, V.-D. Doan, Q.-H. Tran and V. C. Nguyen, Biosynthesis of Zinc Oxide Nanoparticles Using Aqueous *Piper betle* Leaf Extract and Its Application in Surgical Sutures, *J. Nanomater.*, 2021, **2021**, 8833864.
25 N. K. Rajendran, B. P. George, N. N. Houreld and H. Abrahamse, Synthesis of Zinc Oxide Nanoparticles Using Rubus fairholmianus Root Extract and Their Activity against Pathogenic Bacteria, *Molecules*, 2021, **26**(10), 3029.
26 S. Pal, K. Pal, S. Mukherjee, D. Bera, P. Karmakar and D. Sukhen, Green cardamom mediated Phytosynthesis of ZnONPs and validation of its antibacterial and anticancerous potential, *Mater. Res. Express*, 2020, **7**(1), 015068.
27 V. Vinotha, M. Yazhiniprabha, D. S. Raj, S. Mahboob, K. A. Al-Ghanim, F. Al-Misned, *et al.*, Biogenic synthesis of aromatic cardamom-wrapped zinc oxide nanoparticles and their potential antibacterial and mosquito larvicidal activity: An effective eco-friendly approach, *J. Environ. Chem. Eng.*, 2020, **8**(6), 104466.
28 P. Harini, R. Hannah and S. Rajeshkumar, Evaluation of antifungal activity and cytotoxic effects of fruit mediated zinc oxide nanoparticles, *Plant Cell Biotechnol. Mol. Biol.*, 2020, **22**(53–54), 96–105.
29 A. A. Mohammed, K. H. Jawad, S. Çevik, G. M. Sulaiman, S. Albukhaty and P. Sasikumar, Investigating the Antimicrobial, Antioxidant, and Anticancer Effects of Elettaria cardamomum Seed Extract Conjugated to Green Synthesized Silver Nanoparticles by Laser Ablation, *Plasmonics*, 2024, **19**(3), 1187–1200.
30 N. Kadian, R. Kumari, A. Panchal, J. Dalal and D. Padalia, Structural and optical properties of gadolinium doped-magnetite nano-crystal for photocatalytic application, *J. Alloys Compd.*, 2023, **960**, 170811.
31 V. Soshnikova, Y. J. Kim, P. Singh, Y. Huo, J. Markus, S. Ahn, *et al.*, Cardamom fruits as a green resource for facile synthesis of gold and silver nanoparticles and their biological applications, *Artif. Cells, Nanomed., Biotechnol.*, 2018, **46**(1), 108–117.
32 E. V. Rodríguez-Negrete, Á. Morales-González, E. O. Madrigal-Santillán, K. Sánchez-Reyes, I. Álvarez-González and E. Madrigal-Bujaidar, Phytochemicals and Their Usefulness in the Maintenance of Health, *Plants*, 2024, **13**(4), 523.
33 D. V. Navarrete-Carriola, A. D. Paz-González, L. K. Vázquez-Jiménez, E. De Luna-Santillana, M. A. Cruz-Hernández, D. Bandyopadhyay, *et al.*, Comparative Analysis of a Secondary Metabolite Profile from Roots and Leaves of Iostephane heterophylla by UPLC-MS and GC-MS, *ACS Omega*, 2024, **9**(5), 5429–5439.

34 S. Rohilla, A. Gupta, V. Kumar, S. Kumari, M. Petru, N. Amor, M. T. Noman and J. Dalal, Excellent UV-light triggered photocatalytic performance of ZnO. SiO2 nanocomposite for water pollutant compound methyl orange dye, *Nanomaterials*, 2021, **11**(10), 2548.

35 G. Singh, S. Kiran, P. Marimuthu, V. Isidorov and V. Vinogorova, Antioxidant and antimicrobial activities of essential oil and various oleoresins of Elettaria cardamomum (seeds and pods), *J. Sci. Food Agric.*, 2008, **88**(2), 280–289.

36 E. Noumi, M. Snoussi, M. M. Alreshidi, P.-D. Rekha, K. Saptami, L. Caputo, *et al.*, Chemical and biological evaluation of essential oils from cardamom species, 2018, **23**(11), 2818.

37 J. Gaur, S. Kumar, M. Pal, H. Kaur, B. R. Supreet, *et al.*, Bio-engineered, phyto-decorated, multi-form P. betle/ZnO as a potential photocatalytic agent, *Adv. Nat. Sci.:Nanosci. Nanotechnol.*, 2023, **14**(3), 035014.

38 H. Kaur, S. Kumar, S. Kaushal, R. Badru, P. P. Singh and A. Pugazhendhi, Highly customized porous TiO2-PANI nanoparticles with excellent photocatalytic efficiency for dye degradation, *Environ. Res.*, 2023, **225**, 114960.

39 C. Y. Chong, J. Y. Sum, L. S. Lai, P. Y. Toh and Z. H. Chang, Visible light-driven dye degradation by magnetic cobalt-doped zinc oxide/iron oxide photocatalyst, *Next Mater.*, 2024, **2**, 100074.

40 S. Kumari, S. Malik, S. Kumar, J. Dalal, S. Dahiya, A. Ohlan, R. Punia and A. S. Maan, Excellent photoelectrical properties of ZnO thin film based on ZnO/epoxy-resin ink for UV-light detectors, *InAIP Conference Proceedings*, AIP Publishing, 2019 Aug 29, vol. 2142, no. 1.

41 M. F. Islam, S. islam, M. A. S. Miah, A. K. O. Huq, A. K. Saha, Z. J. Mou, *et al.*, Green synthesis of zinc oxide nano particles using Allium cepa L. waste peel extracts and its antioxidant and antibacterial activities, *Heliyon*, 2024, **10**(3), e25430.

42 M. H. Kahsay, A. Tadesse, D. RamaDevi, N. Belachew and K. Basavaiah, Green synthesis of zinc oxide nanostructures and investigation of their photocatalytic and bactericidal applications, *RSC Adv.*, 2019, **9**(63), 36967–36981.

43 M. Ramesh, M. Anbuvannan and G. Viruthagiri, Green synthesis of ZnO nanoparticles using Solanum nigrum leaf extract and their antibacterial activity, *Spectrochim. Acta, Part A*, 2015, **136**, 864–870.

44 R. Yuvakkumar, J. Suresh, A. J. Nathanael, M. Sundrarajan and S. I. Hong, Novel green synthetic strategy to prepare ZnO nanocrystals using rambutan (Nephelium lappaceum L.) peel extract and its antibacterial applications, *Mater. Sci. Eng., C*, 2014, **41**, 17–27.

45 S. T. Karam and A. F. Abdulrahman, Green Synthesis and Characterization of ZnO Nanoparticles by Using Thyme Plant Leaf Extract, *Photonics*, 2022, **9**(8), 594.

46 K. S. K, M. P. N. P and M. Vasundhara, Enhanced photocatalytic activity in ZnO nanoparticles developed using novel Lepidagathis ananthapuramensis leaf extract, *RSC Adv.*, 2023, **13**(3), 1497–1515.

47 H. Cheng, W. Wang, B. Huang, Z. Wang, J. Zhan and X. Qin, Tailoring AgI nanoparticles for the assembly of AgI/BiOI hierarchical hybrids with size-dependent photocatalytic activities, *J. Mater. Chem. A*, 2013, **1**(24), 7131–7136.

48 H. Kaur, S. Kumar, N. K. Verma and P. Singh, Role of pH on the photocatalytic activity of TiO2 tailored by W/T mole ratio, *J. Mater. Sci.: Mater. Electron.*, 2018, **29**(18), 16120–16135.

49 A. S. Abdelbaky, A. M. H. A. Mohamed, M. Sharaky, N. A. Mohamed and Y. M. Diab, Green approach for the synthesis of ZnO nanoparticles using Cymbopogon citratus aqueous leaf extract: characterization and evaluation of their biological activities, *Chem. Biol. Technol. Agric.*, 2023, **10**(1), 63.

50 N. F. Khadiran, M. Z. Hussein, R. Ahmad, T. Khadiran, Z. Zainal, W. R. W. A. Kadir, *et al.*, Preparation and properties of zinc layered hydroxide with nitrate and phosphate as the counter anion, a novel control release fertilizer formulation, *J. Porous Mater.*, 2021, **28**(6), 1797–1811.

51 R. G. Kempegowda, R. B. Gokavi and K. S. Murthy, Banks CEJJoM, Metals, Fuels, *Chemically Modified Screen-Printed Electrodes: an Electrochemical Interface for Nitrite Ions*, 2023, pp. 43–51.

52 A. Rajan, A. R. Rajan and D. Philip, Elettaria cardamomum seed mediated rapid synthesis of gold nanoparticles and its biological activities, *OpenNano*, 2017, **2**, 1–8.

53 T. Bhuyan, K. Mishra, M. Khanuja, R. Prasad and A. Varma, Biosynthesis of zinc oxide nanoparticles from Azadirachta indica for antibacterial and photocatalytic applications, *Mater. Sci. Semicond. Process.*, 2015, **32**, 55–61.

54 M. V. Sujitha and S. Kannan, Green synthesis of gold nanoparticles using Citrus fruits (Citrus limon, Citrus reticulata and Citrus sinensis) aqueous extract and its characterization, *Spectrochim. Acta, Part A*, 2013, **102**, 15–23.

55 D. D. Thongam, J. Gupta and N. K. Sahu, Effect of induced defects on the properties of ZnO nanocrystals: surfactant role and spectroscopic analysis, *SN Appl. Sci.*, 2019, **1**(9), 1030.

56 M. Y. Al-darwesh, S. S. Ibrahim and M. A. Mohammed, A review on plant extract mediated green synthesis of zinc oxide nanoparticles and their biomedical applications, *Results Chem.*, 2024, **7**, 101368.

57 K. Singh and S. Yadav, Biosynthesis of a range of ZnO nanoparticles utilising Salvia hispanica L. seed extract and evaluation of their bioactivity, *Sci. Rep.*, 2025, **15**(1), 4043.

58 E. A. Alzahrani, A. Nabi, M. R. Kamli, S. M. Albukhari, S. A. Althabaiti and S. A. Al-Harbi, Facile Green Synthesis of ZnO NPs and Plasmonic Ag-Supported ZnO Nanocomposite for Photocatalytic Degradation of Methylene Blue, *Water*, 2023, **15**(3), 384.

59 H. Agarwal, S. Venkat Kumar and S. Rajeshkumar, A review on green synthesis of zinc oxide nanoparticles – An eco-friendly approach, *Resour.-Effic. Technol.*, 2017, **3**(4), 406–413.

60 V. Batra, I. Kaur, D. Pathania and C. V. Sonu, Efficient dye degradation strategies using green synthesized ZnO-based nanoplatforms: A review, *Appl. Surf. Sci. Adv.*, 2022, **11**, 100314.

61 A. E. Alprol, A. Eleryan, A. Abouelwafa, A. M. Gad and T. M. Hamad, Green synthesis of zinc oxide nanoparticles using Padina pavonica extract for efficient photocatalytic removal of methylene blue, *Sci. Rep.*, 2024, **14**(1), 32160.

62 A. Kumar, J. Dalal, S. Dahiya, R. Punia, K. D. Sharma, A. Ohlan and A. S. Maan, In situ decoration of silver nanoparticles on single-walled carbon nanotubes by microwave irradiation for enhanced and durable antibacterial finishing on cotton fabric, *Ceram. Int.*, 2019, **45**(1), 1011–1019.

63 M. T. Yassin, A. Abdel-Fattah Mostafa, A. A. Al-Askar and A. S. Alkhelaif, In vitro antimicrobial potency of Elettaria cardamomum ethanolic extract against multidrug resistant of food poisoning bacterial strains, *J. King Saud Univ., Sci.*, 2022, **34**(6), 102167.

64 X. T. Tran, T. T. L. Bien, T. V. Tran and T. T. T. Nguyen, Biosynthesis of ZnO nanoparticles using aqueous extracts of Eclipta prostrata and Piper longum: characterization and assessment of their antioxidant, antibacterial, and photocatalytic properties, *Nanoscale Adv.*, 2024, **6**(19), 4885–4899.

65 A. Bukhari, I. Ijaz, E. Gilani, A. Nazir, H. Zain and R. Saeed, Green Synthesis of Metal and Metal Oxide Nanoparticles Using Different Plants' Parts for Antimicrobial Activity and Anticancer Activity: A Review Article, *Coatings*, 2021, **11**(11), 1374.

66 N. Kaur, J. Singh, S. Kumar, P. Singh, S. Al-Rashed, H. Kaur, *et al.*, An efficient and viable photodegradation of a textile Reactive yellow-86 dye under direct sunlight by multi-structured Fe2O3 encapsulated with phytochemicals of R. indica, *J. Mater. Sci.: Mater. Electron.*, 2020, **31**(23), 21233–21247.

67 B. D. Lade and A. S. Shanware, Phytonanofabrication: methodology and factors affecting biosynthesis of nanoparticles, *Smart Nanosystems for Biomedicine, Optoelectronics and Catalysis*, IntechOpen, 2020.

68 J. Li, Q. Wu and J. Wu. Synthesis of Nanoparticles via Solvothermal and Hydrothermal Methods, in *Handbook of Nanoparticles*, ed. M. Aliofkhazraei, Springer International Publishing, Cham, 2015, pp. 1–28.

69 H. Sadiq, F. Sher, S. Sehar, E. C. Lima, S. Zhang, H. M. N. Iqbal, *et al.*, Green synthesis of ZnO nanoparticles from Syzygium cumini leaves extract with robust photocatalysis applications, *J. Mol. Liq.*, 2021, **335**, 116567.

70 N. F. Ibarra-Cervantes, E. Vázquez-Núñez, C. Gómez-Solis, F. Fernández-Luqueño, G. Basurto-Islas, J. Álvarez-Martínez, *et al.*, Green synthesis of ZnO nanoparticles from ball moss (Tillandsia recurvata) extracts: characterization and evaluation of their photocatalytic activity, *Environ. Sci. Pollut. Res.*, 2024, **31**(9), 13046–13062.

71 J. Gaur, S. Kumar, H. Kaur, M. Pal, B. K. Supreet, *et al.*, Eco-friendly innovation: harnessing nature's blueprint for enhanced photocatalysis and antimicrobial potential in multi-structured PN/ZnO nanoparticles, *Funct. Compos. Struct.*, 2024, **6**(1), 015005.

72 K. Singh, J. Singh and M. Rawat, Green synthesis of zinc oxide nanoparticles using Punica Granatum leaf extract and its application towards photocatalytic degradation of Coomassie brilliant blue R-250 dye, *SN Appl. Sci.*, 2019, **1**(6), 624.

73 J. Gaur, S. Kumar, M. Pal, H. Kaur, R. K. Rana, K. Bala, *et al.*, Bio-functionalized, elongated hexagonal bi-pyramidal, citrus limetta/ZnO nanostructures as potential photocatalytic and seed germinating agents, *Funct. Compos. Struct.*, 2023, **5**(3), 035003.

74 A. M. Rabie, M. R. Abukhadra, A. M. Rady, S. A. Ahmed, A. Labena, H. S. H. Mohamed, *et al.*, Instantaneous photocatalytic degradation of malachite green dye under visible light using novel green Co–ZnO/algae composites, *Res. Chem. Intermed.*, 2020, **46**(3), 1955–1973.

75 S. A. Devi, K. J. Singh and K. N. Devi, A Comparative Study on the Photocatalytic Activity of Eucalyptus Leaf Assisted Green Synthesized ZnO and Chemically Synthesized ZnO towards the Degradation of Malachite Green Dye, *Integr. Ferroelectr.*, 2020, **205**(1), 38–51.

76 H. Kaur, S. Kumar, R. Saini, P. P. Singh and A. Pugazhendhi, One-pot biogenic synthesis of C. limon/TiO2 with dual applications as an advance photocatalyst and antimicrobial agent, *Chemosphere*, 2023, **335**, 139106.

77 A. Ansari, V. U. Siddiqui, W. U. Rehman, M. K. Akram, W. A. Siddiqi and A. M. Alosaimi, Green Synthesis of TiO_2 Nanoparticles Using Acorus calamus Leaf Extract and Evaluating Its Photocatalytic and In Vitro Antimicrobial Activity, *Catalysts*, 2022, **12**(2), 181.

78 J. Singh, H. Kaur, D. Kukkar, V. K. Mukamia, S. Kumar and M. Rawat, Green synthesis of SnO2 NPs for solar light induced photocatalytic applications, *Mater. Res. Express*, 2019, **6**(11), 115007.

79 H. Muthukumar, N. I. Chandrasekaran, M. S. Naina, S. Pichiah and M. Manickam, Iron oxide nano-material: physicochemical traits and in vitro antibacterial propensity against multidrug resistant bacteria, *J. Ind. Eng. Chem.*, 2017, **45**, 121–130.

80 P. Yugandhar, T. Vasavi, B. Shanmugam, P. Uma Maheswari Devi, K. Sathyavelu Reddy and N. Savithramma, Biofabrication, characterization and evaluation of photocatalytic dye degradation efficiency of Syzygium alternifolium leaf extract mediated copper oxide nanoparticles, *Mater. Res. Express*, 2019, **6**(6), 065034.

81 S. Alikarami, A. Soltanizade and F. Rashchi, Photocatalytic activity of the visible-light-driven spherical Ag2S modifying the CdS synthesized by the facile chemical methods for the degradation of methylene blue and rhodamine B, *Mater. Chem. Phys.*, 2022, **285**, 126174.

82 Z. Wei and H. Matsui, Rational strategy for shaped nanomaterial synthesis in reverse micelle reactors, *Nat. Commun.*, 2014, **5**(1), 3870.

83 Y. Chen, R. Huang, D. Chen, Y. Wang, W. Liu, X. Li, *et al.*, Exploring the Different Photocatalytic Performance for Dye Degradations over Hexagonal ZnIn2S4 Microspheres and Cubic ZnIn2S4 Nanoparticles, *ACS Appl. Mater. Interfaces*, 2012, **4**(4), 2273–2279.

84 S. Sultana, S. Mansingh and K. M. Parida, Crystal facet and surface defect engineered low dimensional CeO2 (0D, 1D,

2D) based photocatalytic materials towards energy generation and pollution abatement, *Mater. Adv.*, 2021, **2**(21), 6942–6983.

85 X. Liu, X. Zhang, Y. Liu, M. Liu, X. Miao and Y. Wang, Influence of ZnS crystal morphology on adsorption-photocatalytic efficiency of pseudocrystal ZnS nanomaterials for methylene blue degradation, *J. Mol. Struct.*, 2022, **1256**, 132514.

86 X. Su, D. Fan, H. Sun, J. Yang, Z. Yu, D. Zhang, *et al.*, One-dimensional rod-shaped Ag2Mo2O7/BiOI n-n junctions for efficient photodegradation of tetracycline and rhodamine B under visible light, *J. Alloys Compd.*, 2022, **912**, 165184.

87 X. Zhang, J. Qin, Y. Xue, P. Yu, B. Zhang, L. Wang, *et al.*, Effect of aspect ratio and surface defects on the photocatalytic activity of ZnO nanorods, *Sci. Rep.*, 2014, **4**(1), 4596.

88 A. Das and R. G. Nair, Effect of aspect ratio on photocatalytic performance of hexagonal ZnO nanorods, *J. Alloys Compd.*, 2020, **817**, 153277.

89 M. M. Naik, M. S. Prabhu, S. N. Samant, P. M. Naik and S. Shirodkar, Synergistic Action of Silver Nanoparticles Synthesized from Silver Resistant Estuarine Pseudomonas aeruginosa Strain SN5 with Antibiotics against Antibiotic Resistant Bacterial Human Pathogens, *Thalassas*, 2017, **33**(1), 73–80.

90 Y. Y. Loo, Y. Rukayadi, M.-A.-R. Nor-Khaizura, C. H. Kuan, B. W. Chieng, M. Nishibuchi, *et al.*, In vitro antimicrobial activity of green synthesized silver nanoparticles against selected gram-negative foodborne pathogens, 2018, **9**, 1555.